Made available by Hasselt University Library in https://documentserver.uhasselt.be

Fabrication and characterization smart gold-polymer nanostructure as promising theranostic agent for dual-imaging and chemo-photothermal therapy of cancer: An in vitro study

Peer-reviewed author version

Azizi, M; Pakravan, A; Valizadeh, H; Rahbarghazi, R; Dianat-Moghadam, H; Bani, F; KAHROBA, Houman; Salehi, R & Mehrmohammadi, M (2024) Fabrication and characterization smart gold-polymer nanostructure as promising theranostic agent for dual-imaging and chemo-photothermal therapy of cancer: An in vitro study. In: Journal of Photochemistry and Photobiology A-chemistry, 450 (Art N° 115459).

DOI: 10.1016/j.jphotochem.2024.115459
Handle: http://hdl.handle.net/1942/46302

Fabrication and Characterization Smart Gold-polymer nanostructure as promising theranostic agent for dual-imaging and chemo-photothermal therapy of cancer: An in vitro study

Mehdi Azizi[1,2], Asrin Pakravan[3], Hadi Valizadeh[4], Reza Rahbarghazi[5,6],Hassan Dianat-Moghadam[7], Farhad Bani[8], Houman Kahroba[9,10], Roya Salehi[11*], and Mohammad Mehrmohammadi[12*]

[1]Proteomics Research Center, and Department of Medical Nanotechnology, Faculty of Advanced Medical Sciences, Tabriz University of Medical Sciences, Tabriz, Iran

[2]Department of Tissue Engineering and Biomaterials, School of Advanced Medical Sciences and Technologies, Hamadan University of Medical Sciences, Hamadan, Iran

[3]Chemistry Department, Faculty of Science, Azerbaijan Shahid Madani University, Tabriz, Iran

[4]Department of Pharmaceutics, Faculty of Pharmacy, Tabriz University of Medical Sciences, Tabriz, Iran

[5]Stem Cell Research Center, Tabriz University of Medical Sciences, Tabriz, Iran

[6]Department of Applied Cell Sciences, Faculty of Advanced Medical Sciences, Tabriz University of Medical Sciences, Tabriz, Iran

[7]Department of Medical Biotechnology, Faculty of Advanced Medical Sciences, Tabriz University of Medical Sciences, Tabriz, Iran

[8]Department of Medical Nanotechnology, Faculty of Advanced Medical Sciences, Tabriz University of Medical Sciences, Tabriz, Iran

[9]Department of Toxicogenomics, GROW School for Oncology and Department Biology, Maastricht University, the Netherlands

[10]Center for Environmental Science, Hasselt University, Hasselt, Belgium

[11]Drug Applied Research Center and Department of Medical Nanotechnology, Faculty of Advanced Medical Sciences, Tabriz University of Medical Sciences, Tabriz, Iran

[12]Department of Biomedical Engineering and Department of Obstetrics and Gynecology, Wayne State University, Detroit, Michigan 48201, United States; Barbara Ann Karmanos Cancer Institute, Detroit, Michigan 48201, United States.

Corresponding authors **Roya Salehi,** Email: Salehiro@tbzmed.ac.ir; **Mohammad Mehrmohammadi,** Email: mehr@wayne.edu.

Abstract

In order to enhance the effectiveness of cancer therapy, it is essential to have highly sensitive imaging techniques that provide accurate results. This is crucial for timely diagnosis and the selection of appropriate therapeutic strategies. Despite recent advances in technologies associated with tumor imaging, the application of conventional single-mode imaging is the subject of debate. Herein, a nanostructure with theranostic properties (GNSs-MTX@CD-Pol) was designed from a pH-responsive polymer (Pol), gold nanostar (GNSs), carbon dot (CD), and methotrexate (MTX). Dual-imaging modalities (fluorescence and CT imaging) and synergistic chemo-photothermal therapy were examined in human breast cancer MDA-MB 231 cells.

MTT assay showed NIR irradiation of cells pre-treated with synthesized nanoparticles promoted tumoricidal synergy via the reduction of survival rate after 48 hours compared with the control group ($p<0.05$), indicating a high absorption coefficient in the NIR area and efficient heat production rate. Flow cytometry, real-time PCR, and western blot analyses showed an activation of intrinsic and extrinsic apoptosis pathways inside the host cells. The elevation of p27 and p53 showed apoptotic changes and inhibition of dynamic cell growth compared to the non-treated cells ($p<0.05$). Evident fluorescence intensity at lower pH values (6.3) showed pH-dependent activity of nanoparticle. Furthermore, result was shown that GNSs-MTX@CD-Pol nanostructure has an excellent capability for CT imaging. Overall, all data show that designed novel nanostructure has considerable ability in theranostic applications.

Keywords: *Gold-Polymer Nanostructures; Theranostic; Chemo-Photothermal Therapy; Dual-Imaging Modality; Tumoricidal Effects*

1. Introduction

Until recently, cancer prevention, diagnosis, and therapy domains have traditionally been seen as distinct entities. The limited collaboration between these disciplines has impeded the efficacy of cancer therapy [1]. In light of this, a pressing need has emerged to develop a novel strategies that integrates the diagnosis and therapies of cancer into a unified approach. The field of theranostic nanomedicine has generated considerable interest in using iron oxide, quantum dots, silica, and gold nanoparticles (GNPs) for imaging and therapeutic purposes. The word theranostic is attributed to integrating diagnostic and therapeutic strategies with the rationale of increased safety and efficacy in each cancer patient [2]. The paradigm in cancer cases and therapy has been changed from the classical conventional therapeutic look towards personalized medicine using theranostic [3]. Smart or responsive theranostics are platforms where the therapeutic agent is ideally released/activated only after reaching the target tissue in response to a specific stimulus. Pathological conditions at the target sites can cause these stimuli compared to healthy tissues, such as changes in the pH, redox environment, overexpression of enzymes, or hypoxic conditions [4].

The cellular uptake of therapeutic and imaging agents can be enhanced by manipulating nanoparticles' size, content, shape, and surface properties [5-7]. Despite recent developments in our knowledge about cancer biology, many cancer cases are diagnosed in the end stages because of conventional detection systems' poor sensitivity and specificity, leading to a diminished survival rate [8]. As a correlate, nanocarriers with passive or active targeting abilities have been developed

for the early-stage detection and therapy of multiple cancer types. It was suggested that these nanocarriers would be eligible to raise the half-lives of therapeutic agents in the circulation system and accelerate passive distribution into the tumor niche via EPR mechanisms [9]. Compared to available monotherapies, the simultaneous application of chemotherapeutic agents with other modalities, such as radiation, genetic manipulation, and photothermal irradiation, enables us to suppress tumor development and expansion efficiently [10-12].

Among them, tumoricidal properties of chemo-photothermal therapy have been proved in the clinical setting [13]. It is postulated that coupling photothermal irradiation with chemotherapy yields a synergistic effect. The mild to moderate hyperthermia generated by outer stimulus (laser) promotes coagulation in tumor blood vessels, reducing cell resistance against drugs. In this regard, the NIR laser is touted as a standard stimulus for heat generation. The exposure of distinct nanostructures, such as GNPs, Cu-based nanostructures, and carbon nanotubes, to NIR-based photothermal therapy (PTT) supports a low-risk treatment [14-16]. Among those nanostructures, GNPs have been widely employed in various applications such as drug administration, cell targeting, sensing, and molecular imaging of cancer cells. Because of their biological inertness, superior optical properties, non-toxicity and biocompatibility, and chemically modifiable surface, GNPs pave the way for reliable multifunctional platforms for developing cancer nanotheranostics [17-19]. Also, GNPs have the potential to efficiently scatter or absorb light at a tunable resonance frequency, named localized surface plasmon resonance (LSPR). The LSPR properties enriched contrast for various optical imaging modalities containing computerized tomography (CT), photoacoustic (PAT), and multi-photon photoluminescence imaging [20].

Previously, a new type of MTX-driven (methotrexate as an anticancer drug and analog of folic acid for folate receptor targeting) carbon dot was synthesized by our research group for self-targeting, imaging, and therapy of cancer cells [21]. Herein, we developed a novel smart theranostic system based on an ultra pH-sensitive copolymer composed of poly (ethylene glycol)-b-poly [2 (diisopropylamino) ethyl methacrylate-co-2-aminoethyl methacrylate (AEMA)] copolymer, (PEG-b-(P DiPAEMA-co-AEMA) with atom transfer radical polymerization. Then, gold nanostars (GNSs) were fabricated and conjugated with MTX as a targeting and chemotherapy agent (GNSs-MTX). GNSs, as a quencher, were conjugated with an imaging fluorochrome MTX-derivative carbon dots (MTX-CDs) via PEG-b-P (DiPAEMA-co-AEMA) copolymer to develop multifunctional GNS-MTX@CD-Pol NSs. Both pH-responsive and tumoricidal properties of GNSs-MTX@CD-Pol NSs were investigated in human MDA-MB 231 breast cancer cells in combination with their PTT effect.

2. Material and Methods

2.1. Materials

$HAuCl_4$ (≥99.9%), RB, MTT, PI, MTX, PMDETA, DiPAEMA, AEMA, EDC/NHS, 2-bromo-2-methyl propanoyl bromide, MeO-PEG_{114}-OH, DMAP, TEA, CTAB, $NaBH_4$, PVP, (Mw=40000 g/mol) and CuBr were purchased from Sigma-Aldrich. CuBr was suspended for 12 hours with an excess of glacial acetic acid, filtered and washed with absolute ethyl alcohol followed by anhydrous ethyl ether. The purified CuBr was vacuum dried at 80˚C for 48 hours and stored under nitrogen at 4˚C. Sodium citrate ($Na_3C_6H_5O_7$. $2H_2O$, >99%), $AgNO_3$, AA, HCl, NaCl, NaBr, and Na_2S (55%) were purchased from Merck Co and used without further purification. Deionized water (resistance >18.2 MΩ) was used in all experiments. Other materials used in biological protocols, including Penicillin-Streptomycin, FBS, Ribonuclease (RNase),

Trypsin-EDTA, and RPMI, were obtained from Gibco BRL Life Technologies. To assess apoptosis, we purchased an apoptosis kit (ApoFlowEx® FITC Kit) from Exbio Inc.

2.2. Apparatus and Characterization

The optical behavior of synthesized GNSs was analyzed with a double-beam PC 1601 UV–Vis (SHIMADZU, Kyoto, Japan) spectrophotometer. TEM imaging [(TEM; LEO 906 TEM (Germany, Zeiss)] was performed at 100Kv acceleration voltages to investigate GNSs particle size and morphology. DLS and zeta potential (ζ) (DLS; Nano-ZS, Malvern Instruments (Malvern, UK) were utilized to measure GNSs particle size and zeta potential values. ^{1}H NMR spectra were recorded on an FT-NMR Bruker spectrometer (Bruker, Ettlingen, Germany) with an operating frequency of 400 MHz at 25°C. FT-IR spectra were recorded on Bruker (Tensor 27) IR spectrophotometer instrument. Other analyses, such as ICP-MS (Elan 6100DRC-e, Perkin-Elmer, Waltham, MA, USA), were applied to evaluate gold ion concentration and quantify GNSs uptake by MDA-MB 231 cells. GPC analysis was achieved with Shimadzu LC20A instrument using Waters Ultra-hydrogel linear column (exclusion limit 0.2 to 80 KDa) and 0.1 M $NaNO_3$ in water as mobile phase with the flow rate of 0.9 ml/min, the temperature of 35˚C.

2.3 Methods:

2.3.1 Synthesis of GNSs

GNSs were synthesized using a seed-mediated growth two-step technique described previously [22]. The gold nanoparticles with an approximate size of 13 nm

were synthesized with the turkevich method. The procedure was followed by the surfactant-free method [23].

2.3.2 Synthesis of PEG_{114}-b-P (DiPAEMA-co-AEMA)

PEG macro-initiator (MeO-PEG_{114}-Br) was obtained just as the method described below. To activate MeO-PEG_{114}-OH, we dissolved 0.92 g of DMAP in dry THF. After adding 0.7 ml of TEA to the solution, the components were added to a three-necked balloon under dry argon atmosphere flow. Of note, 12.5 g of MeO-PEG-OH was dissolved in 50 ml of dry THF and added dropwise to the three-necked balloon. An ice bath set the balloon's temperature at zero degrees. After this step, 1.54 ml of 2-bromo-isobutyl bromide dissolved in 10 ml of dry THF and slowly added to the three-necked balloon using a syringe. After adding all the components, the color of the solution transformed to pale yellow. The above solution was stirred under argon flow at 280 rpm for 18 hours until the reaction was completed. Then, the obtained product was filtered, and the residue was placed at RT for complete drying [24]. Final polymers were synthesized by the ATRP method. To this end, 1.71 g DiPAEMA (8 mmol), 100 mg AMA (0.6 mmol), 21 µl PMDETA (0.1 mmol), and 0.5 g MeO-PEG_{114}-Br (0.1 mmol) were dissolved in solvent mixed (2-propanol (2 ml) and DMF (2 ml)) and poured in a polymerization tube. Dissolved oxygen was removed by three cycles of freeze-pump-thaw. Then 14.4 mg CuBr (0.1 mmol) was added into the reaction tube under a nitrogen flow, and the tube was sealed in vacuo. The polymerization was done at 40°C for 12 hours. After the completion of the polymerization step, the reaction mixture was diluted with 10 ml THF and dialyzed to remove the catalyst. The solvent was eliminated by a rotary evaporator (Heidolph, Germany). The product was dialyzed in distilled water and lyophilized to obtain a white powder.

2.3.3 Synthesis of PEG_{114}-b-P (DiPAMA-co-AEMA-r-CD)

EDC/NHS activated CDs for 48 hours. After that, 50 mg PEG_{114}-b-P (DiPAMA-co-AEMA) dissolved in 2 ml of anhydrous DMF, followed by the addition of an activated CD, and stirred at RT for two consecutive days. The synthesized polymers were purified by dialyze bag to eliminate the free CDs, lyophilized, and stored at -20°C.

2.3.4 MTX loading on GNSs and self-assemble of GNSs-MTX@CD-Pol

For drug loading, 5 µl (25 mM) MTX was added to 500 µl of 100 ppm GNSs and stirred overnight at RT. Unbound MTX was removed from the mixture by centrifuging at 10,000 rpm for 10 minutes. The procedure was followed by washing with 10 mM phosphate buffer (pH=7.2) three times [25]. Next, 150 µl of PEG-b-P(DiPAEMA-co-AEMA-r-CD) (1 mg/ml) dissolved in DMF was added to 8500 µl GNSs-MTX solution (50 ppm, in DMF) under vigorous stirring. Then, 0.3 ml of Tris-HCl was added dropwise at RT. After that, 20 µl dodecanethiol solution (20 µl in 2 mL of DMF) was added and stirred for 1 hour. Another 3 mL of Tris-HCl was added dropwise to the mixture. The organic solvent was eliminated by dialysis using PBS for 24 hours. Lastly, the solution in the dialysis bag was centrifuged at 10000 rpm for 10 minutes. The copolymer-decorated GNSs were re-dispersed in 1 ml of PBS (pH= 7.4) [26].

2.3.5 Photothermal procedure

To test whether GNSs and GNSs-MTX@CD-Pol can exhibit efficient photothermal effects, 50 µg/ml GNSs and GNSs-MTX@CD-Pol were dissolved in PBS. Then, 200 µl of each solution was poured into a well of 96-well plates. The plates were exposed to continuous-wave NIR laser Diode (λ=808 nm; 2.5 W, Model: PSU-III-LED, Changchun new institute, China) at a power density of 0.7 W/cm^{-2} at

different time points including 2, 4, 6, 8, and 10 minutes. The PBS temperature was monitored throughout irradiation using a digital thermocouple (LCD K-Type Digital Thermometer, Model: TM-902C w Thermocouple Wire, Shenzhen, China) immersed directly into suspensions. Temperature rises of the suspensions were recorded as a function of the irradiation time, and initial points for all of the nanostructure were recorded as t=0.

2.3.6 Cell viability assay

The tumoricidal effects of GNSs and GNSs-MTX@CD-Pol were assessed using conventional MTT assay. For this purpose, human breast cancer MDA-MB 231 cells were seeded in 96-well culture plates at an initial density of 1×10^4 cells per well. Cells were suspended in RPMI1640 medium supplemented with 10% FBS and 1% Penicillin/Streptomycin and kept at standard culture condition (37°C with 5% CO_2). Upon reaching 70% confluence, cells were treated with concentrations (ranging from 0 to 100 µg/ml) of GNSs and GNSs-MTX@CD-Pol for 24 hours. Untreated cells were considered as the control group. After completion of incubation time, the culture medium was discarded, and cells were washed two times with PBS. Then, 200 µl MTT solution (5 mg/ml) was added to each well, and plates were retained at 37˚C for 4 hours. After discarding the supernatant, 200 µl of DMSO was added to dissolve formazan crystals. Lastly, the optical densities of every well were assessed by an ELISA plate reader (Awareness Technology, Palm City, FL, USA) at 570 nm with a reference wavelength of 630 nm. All measurements were performed in triplicate, and statistical analysis was done using OriginPro software.

2.3.7 Photothermal effects on cells pre-treated with GNSs and GNSs-MTX@CD-Pol

To this end, MDA-MB 231 cells were cultured in 96-well plates and pretreated with 50 µg/ml GNSs and GNSs-MTX@CD-Pol for 3 hours. The supernatant was discarded, and cells were washed three times with PBS to eliminate the free formulations. Cells were then exposed to NIR light at recommended doses. This study considered irradiated cells without GNSs treatment as a positive control group. The cytotoxicity of each group was measured by MTT assay.

2.3.8 In vitro cell uptake of GNSs and GNSs-MTX@CD-Pol

2.3.8.1 ICP-MS analysis of cell uptake

To this end, 5×10^5 MDA-MB 231 cells were seeded per well of 6-well plates (24 h) and incubated with GNSs and GNSs-MTX@CD-Pol for 4 hours. Following PBS washes, cells were trypsinized, counted, and digested in concentrated HNO_3 for 1 hour at 90–100°C. The suspension was recovered and diluted in 1% HCl, and the Au extent was obtained by ICP-MS as previously described [27, 28].

2.3.8.2 Flow cytometric analysis of cell uptake

Quantitative analysis of GNSs and GNSs-MTX@CD-Pol uptake was done using flow cytometry. In brief, 1 ml of nanostructures were mixed with 200 µl of RhoB in PBS and stirred overnight at RT in dark conditions. Afterward, RhoB-loaded GNSs and GNSs-MTX@CD-Pol were separated using Amicon® Ultra Centrifugal filters with a molecular cut-off 50KDa. To eliminate unloaded RhoB, the precipitates were washed several times with PBS. For the flow cytometry analysis, 5×10^5 cells/well MDA-MB 231 cells were seeded onto coverslips in 6-well culture plates and incubated for 24 hours at 37°C. 2 ml culture medium containing RhoB-labeled nanostructures at a concentration of IC_{50} was poured into each well and cell

incubated with 1 and 4 hours. Non-treated cells were considered as a negative control. Finally, cells were collected and investigated using a BD® FACSCalibur flow cytometer (USA).

2.3.9 Dual-modality CT and fluorescence imaging of cancer cells

For this purpose, MDA-MB 231 cells were seeded onto culture dishes at a density of 2×10^6 cells per plate and cultured for 24 h at 37 °C and 5% CO_2. Then cells were incubated for 3 hours in a culture medium containing 50 µg/ml of GNSs-MTX@CD-Pol, following PBS wash, dual-modality CT and fluorescence imaging were performed. CT images were captured by a CT imaging system with 50 kVp, 0.800 mA, and fluorescence imaging was done using Plan Apo apochromatic objectives (Nikon, Tokyo, Japan) and a fluorescence microscope (Olympus microscope Bh2-FCA, Japan). The best fluorescence excitation was detected while mirror cube units were adjusted for 480–510 and 510–550 nm.

2.3.10 Cell cycle analysis

Following 3-hour incubation of MDA-MB 231 cells with 50 µg/ml of GNSs and GNSs-MTX@CD-Pol and exposure to laser irradiation, cells were kept for the next 48 hours, and collected for cell cycle analysis. In short, cells were fixed in 70% ice-cold ethanol, incubated with ribonuclease solution, stained with PI solution, and analyzed with FACSCalibur flow cytometer [29].

2.3.11 Flow cytometric analysis of apoptosis

Following 3-hour incubation of MDA-MB 231 cells with 50 µg/ml GNSs and GNSs-MTX@CD-Pol and exposure to laser irradiation, cells were kept for the next 48 hours. Then, cells were collected using Trypsin-EDTA, washed with PBS, and incubated in 1X Annexin binding buffer. According to the manufacturer's instruction,

suspensions were incubated in a binding buffer containing 5 µl Annexin-V and 5 µl PI for cell staining. The percent of cells with early and late apoptotic changes was calculated using a flow cytometry system.

2.3.12 Real-time PCR (RT-qPCR) analysis

The expression of different genes related to apoptosis, such as CASPASE-3, 6, 7, 8, 9, 10, 12, Bax, and Bcl-2, was monitored in the treated cells (with 50 µg/ml GNSs and GNSs-MTX@CD-Pol and exposure to laser irradiation) using real-time PCR analysis. Total RNA content was extracted from different groups using the TRIzol® method [30]. NanoDrop Spectrophotometer determined the integrity and content of RNA. The extracted RNA was reverse-transcribed into cDNA by a reverse transcription Kit (Bioneer, Korea). RT-qPCR was achieved by QuantiTect SYRB Green dye (TaKaRa, Japan) and Corbett Rotor-Gene™ 6000 HRM system. RT-qPCR primer sequences were outlined in **Table 1** according to our previously published data [30, 31]. The expression amount of each gene was investigated by the Pfafl technique with normalization to the housekeeping gene, Glyceraldehyde-3-Phosphate Dehydrogenase (GAPDH).

Table 1. mRNA primers for real-time PCR.

Gene	Forward primer	Reverse primer	Tm(˚C)
CASPASE-3	GAAATTGTGGAATTGATGCGTGA	CTACAACGATCCCCTCTGAAAAA	60
CASPASE-6	ATGGCGAAGGCAATCACATTT	GTGCTGGTTTCCCCGACAT	60
CASPASE-7	AGGGACCGAGCTTGATGATG	CACTGGGATCTTGTATCGAGGA	60
CASPASE-8	GATCAAGCCCCACGATGAC	CCTGTCCATCAGTGCCATAG	60
CASPASE-9	CTTCGTTTCTGCGAACTAACAGG	GCACCACTGGGGTAAGGTTT	60
CASPASE-10	AGAAACCTGCTCTACGAACTGT	GGGAAGCGAGTCTTTCAGAAG	60
CASPASE-12	TGTTACAAAGGCTCATGTGGAAA	GGGTCAGTATATTTGGGGTCTCA	60

Bax	TTCTGACGGCAACTTCAACT	CAGCCCATGATGGTTCTGAT	60
Bcl-2	GGGAATCGATCTGGAAATCCTC	GGCAACGATCCCATCAATCT	60
GAPDH	ACAACTTTGGTATCGTGGAAGG	GCCATCACGCCACAGTTTC	60

2.3.13 Western blotting

In line with gene expression analysis, protein levels of Caspase 3, 9, P53, P27, Bax, and Bcl-2 were investigated using western blotting. After completion of the experimental procedure, MDA-MB 231 cells were lysed using protein lysis buffer (25 mM HEPES, 1% Triton X-100, 2 mM EDTA, 0.1 mM NaCl, 25 mM NaF, and 1 mM Sodium Orthovanadate) enriched with protease cocktail inhibitor (Roche). Samples were kept on ice for 30 minutes and then were vortexed. Cell lysates were centrifuged at 12000 g for 20 minutes. The supernatants were collected and the contents were determined using Picodrop (Cambridge, UK). An equal amount of protein (~100 µg) was separated using 10% SDS-PAGE and transferred onto the PVDF membrane. Skim milk (5%) was used to block non-specific binding sites and membranes were incubated with antibodies against Caspase 3, 9, P53, P27, Bax, and Bcl-2 (all purchased from Santa Cruz Biotechnology Inc., USA) for 1 hour at RT. Immuno-reactive bands were visualized using ECL reagent (BioRad) and X-ray films. The density of each band was determined using Image J software (version 1.4; NIH).

3. Result and Discussion

3.1 Synthesis and characterization of pH-responsive and self-assembled GNSs probes

We constructed the multifunctional GNS and were coated with pH-sensitive PEG-b-P (DiPAEMA-co-AEMA-r-CD) (Pol-CD@GNSs-MTX). The GNSs were synthesized using galvanic replacement methods. TEM imaging reveals an average size of gold nanoparticles (seed-mediated source), GNSs, and Pol-CD@GNSs-MTX

(Figure 1). According to LSPR spectroscopy, maximum absorption peaks were in the wavelength of 768 nm before polymer coating **(Figure 1).** The hydrodynamic diameter of the as-prepared GNSs was about 116 nm. Zeta potential values reached 24.3 mV in an aqueous solution **(Table 2 and Figure 2).** The dodecanethiol and MTX were used to cover GNSs, making the GNSs core hydrophobic to trigger the self-assembly of the copolymer onto the GNSs-MTX as targeting and drug agent (as an analog of folic acid to folate receptor targeting), respectively. Our data shows that the MTX amount in MTX-GNSs was 0.93 µg/ml.

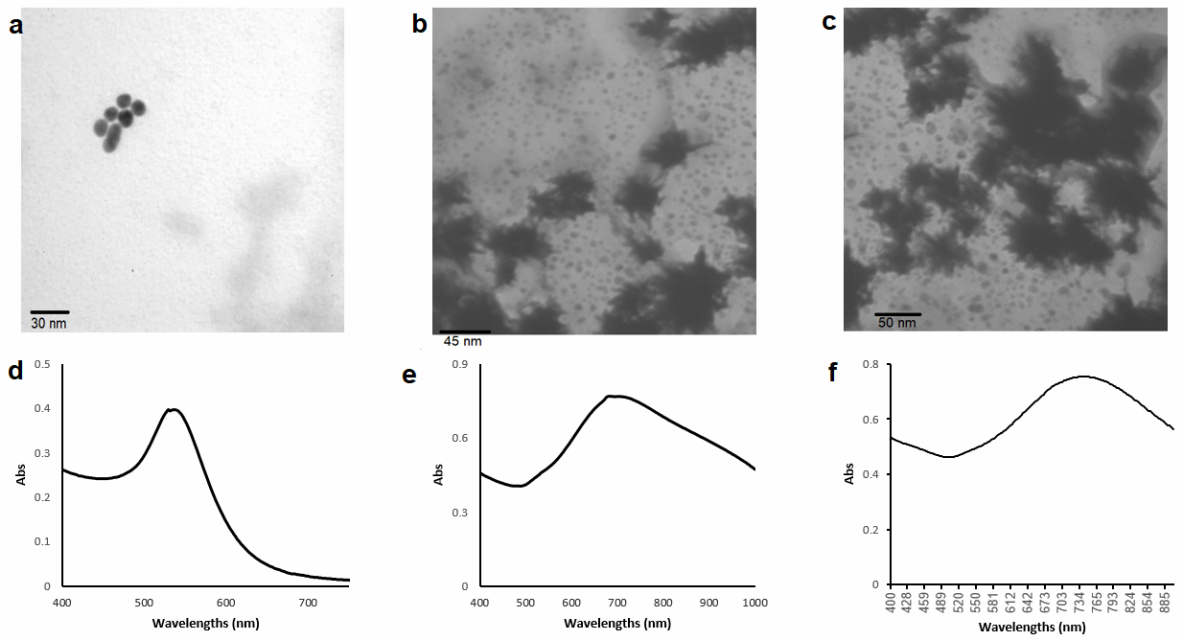

Figure 1.TEM images and UV-Vis spectroscopy of synthesized GNSs and Pol-CD@GNSs-MTX. **(a)** GNPs (seed source for GNSs synthesis) with an average size of 17± 3.2 nm. **(b)** GNSs with an average size of 43.2 ± 8.2 nm. **(c)** Pol-CD@GNSs-MTX with an average size of 49.6 ± 7.1 nm. UV-Vis spectra of **(d)** GNPs, **(e)** GNSs, and (**f)** Pol-CD@GNSs-MTX. The maximum absorption of GNPs, GNSs, and Pol-CD@GNSs-MTX was about 534, 726, and 756 nm, respectively.

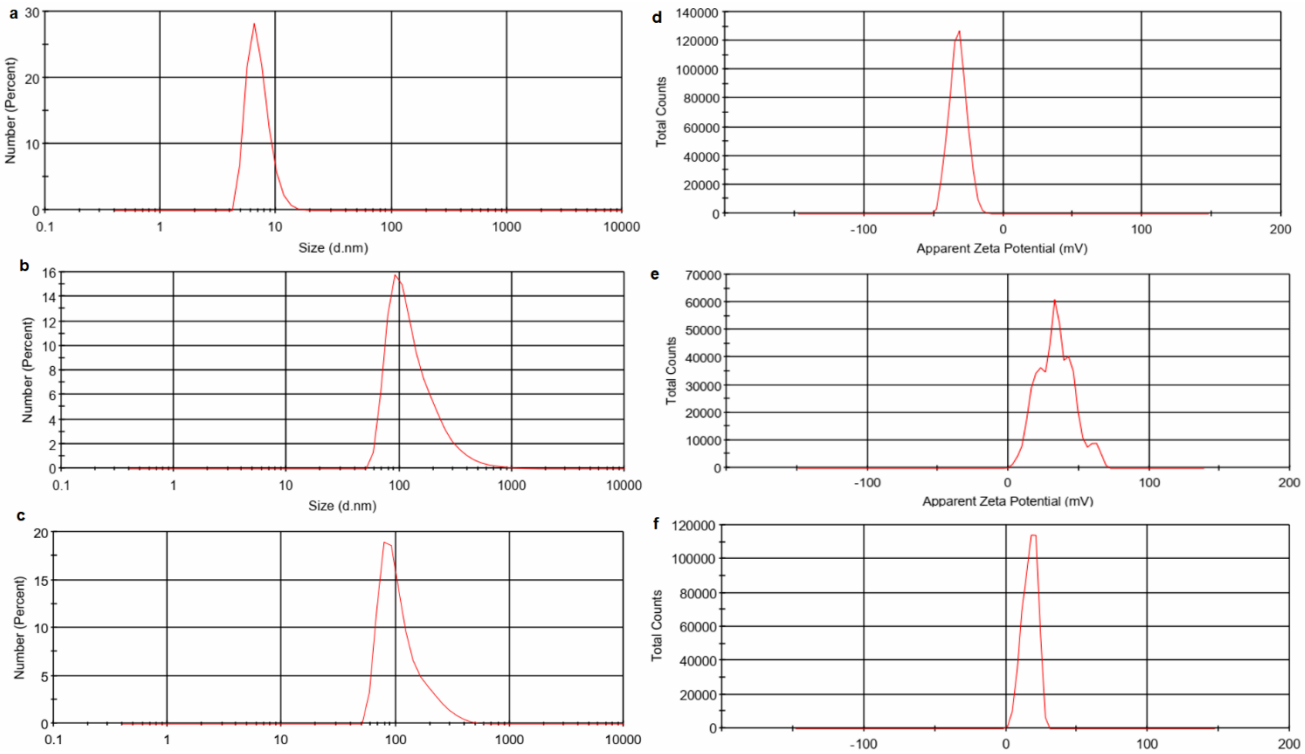

Figure 2. Size distribution and zeta potential of synthesized nanostructures. (a) GNPs, **(b)** GNSs, and **(c)** Pol-CD@GNSs-MTX show the Size distribution; **(d)** GNPs, **(e)** GNSs, and **(f)** Pol-CD@GNSs-MTX show zeta potential.

Table 2. Hydrodynamic diameter, PDI, and Zeta potential of GNPs, GNSs, and Pol-CD@GNSs-MTX.

Structures	Size (nm)	PDI	Zeta potential (mV)
GNPs	49.19	0.621	**-32.5**
GNSs	116	0.493	24.3
GNSs-MTX@CD-Pol	143	0.4	16.9

We synthesized a pH-responsive copolymer using the ATRP method in the next step [26]. The scheme of the synthesis of MeO-PEG_{114}-Br and PEG_{114}-b-P (DiPAEMA-co-AEMA) is shown in **Figure 3 and 4**. The chemical structure of the MeO-PEG_{114}-Br and P PEG_{114}-b-P (DiPAEMA-co-AEMA) was analyzed by ^{1}HNMR using $CDCl_3$ as the solvent **Figure 3 and 4** and FTIR spectroscopy **(Figure 5).** The characteristic peaks of MeO-PEG_{114}-Br moiety were observed at δ=3.6-3.8 ppm (t, 4H, (-OC$\underline{H}_2$-C$\underline{H}_2$-O)

and δ=1.97ppm (s, 6H, C($C\underline{H}_3$)Br. The chemical shifts of the DIPAEMA segment appeared at δ=4.3 ppm (t, 2H, O=C-O($C\underline{H}_2$)), δ=3.5 ppm (t, 2H, $C\underline{H}_2$-N($CH(CH_3)_2$), δ=1.79 ppm (s, 2H, N($C\underline{H}(CH_3)_2$) and δ=3.38 ppm (s, 12H, N($CH(C\underline{H}_3)_2)_2$). The characteristic peaks related to the AEMA moiety of the copolymer were observed at δ=3.82 ppm (t, 2H, $C\underline{H}_2$-NH_2) and δ=5.26 ppm (2H, CH_2-$N\underline{H}_2$). Finally, peaks at 1.4 and 1.6 ppm were related to polymer backbone protons. Synthesized PEG_{114}-b-P(DiPAEMA-co-AEMA) was also characterized by FTIR spectroscopy **(Figure 5).** A signal at 1112 cm^{-1} was related to the stretching vibration of the eteric C-O-C parts of the copolymer. Moreover, the strong peaks at 2888 and 1350 cm^{-1} are associated with the aliphatic C-H stretching and bending mode, respectively. The absorption band at 1736 cm^{-1} was related to the stretching vibration of esteric carbonyl (C=O) copolymer groups. The peak at 3449 cm^{-1} correlated to the stretching vibration of N-H groups in AEMA. Molecular weights (Mn and Mw) and polydispersity index (PDI) copolymer obtained by GPC were 9362 Daltons, 8429 Daltons, and 1.11, respectively **(Figure 6).** The predicted molecular weight obtained by ^{1}HNMR spectroscopy was around 9855 Daltons. This co-polymer was composed of PEG, which functioned as a maintaining of colloidal dispersity of GNSs in aqueous solutions and hydrophobicity switchable block bear of TA. In the current study, DiPAEMA was employed to the TA segment's hydrophobicity and adjust the pKa value (6.2-6.4). To monitor the reversible pH-responsivity, an MTX-CD dye [21] was conjugated to the P(DiPAEMA-co-AEMA) copolymer as an imaging agents, producing PEG-b P(DiPAEMA-co-AEMA-r-CD). The TA groups were thought to be deprotonated, and the segments became hydrophobic in normal tissue conditions (pH 7.4). The MTX-CDs dyes were close to the GNSs, so their fluorescence was effectively quenched. In final self-assembled nanostructures, absorption bands of

GNSs red-shift in the UV-Vis spectra. TEM images disclosed the core-shell structures of synthesized nano-assemblies with a nearly 5 nm thickness surrounding the GNSs cores **(Figure 1).** The hydrodynamic diameter and zeta potential of Pol-CD@GNSs-MTX were 143 nm and 16.9 mV, respectively **(Table. 2 and Figure 2).**

a)

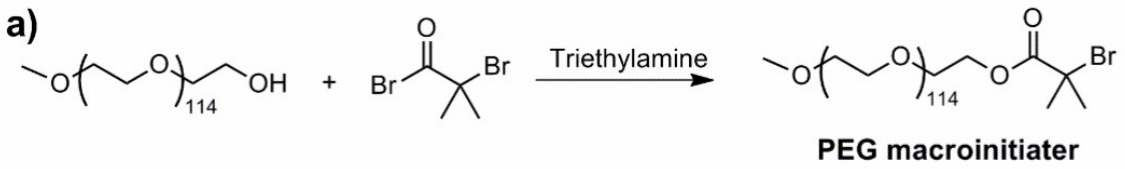

b)

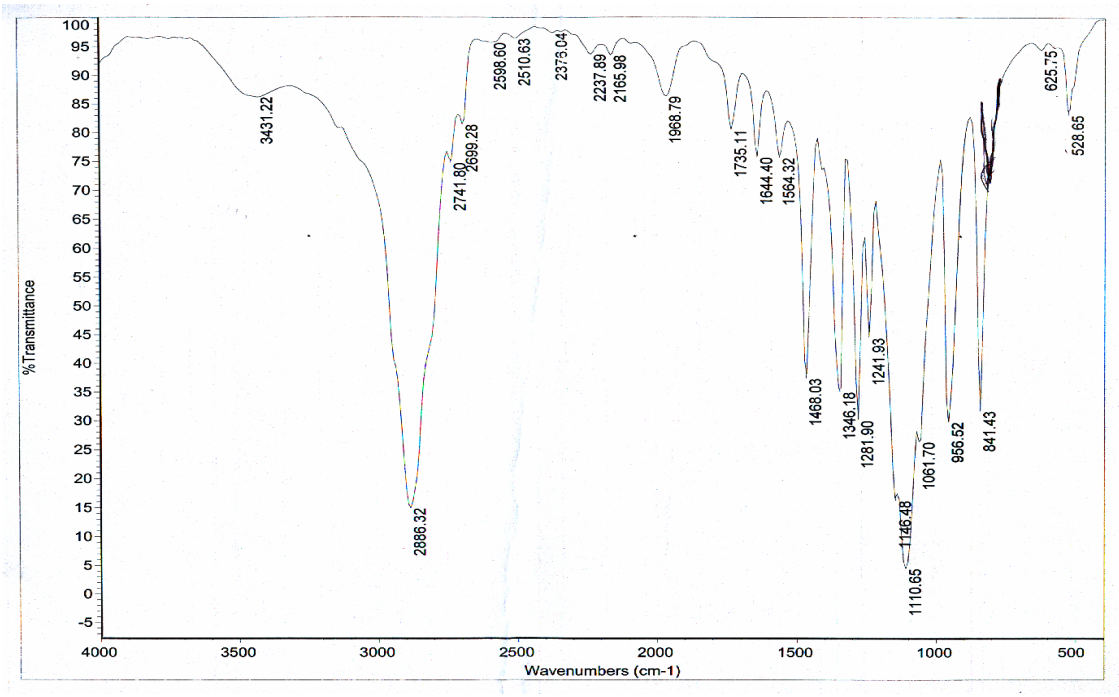

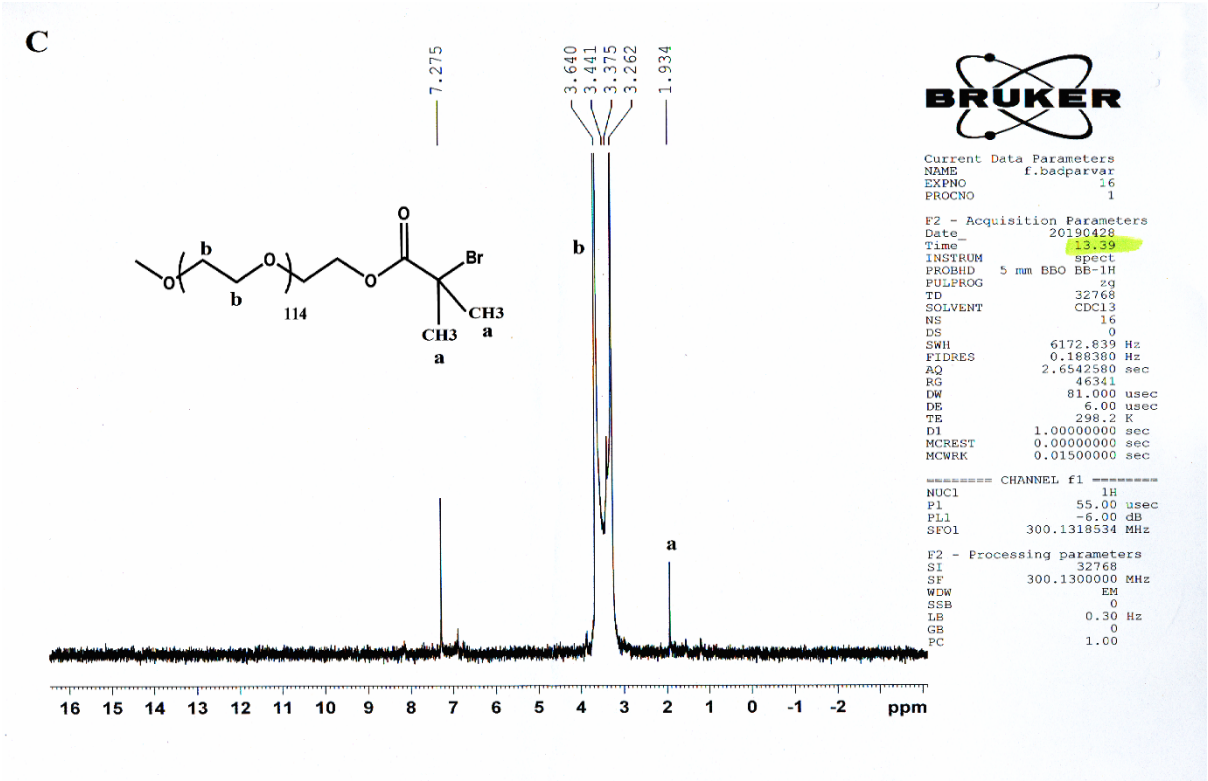

Figure 3. a) Synthetic route of PEG macroinitiator. b. FT-IR spectroscopy of PEG macroinitiator. c) ^{1}H NMR spectrum of the PEG macroinitiator (D_2O, 400 MHz, ppm): δ 1.93 (s, 6H, -C(O)C(CH_3)$_2$Br), 3.36 (s, 3H, CH_3O), 3.68 (m, 450H, OCH_2CH_2O).

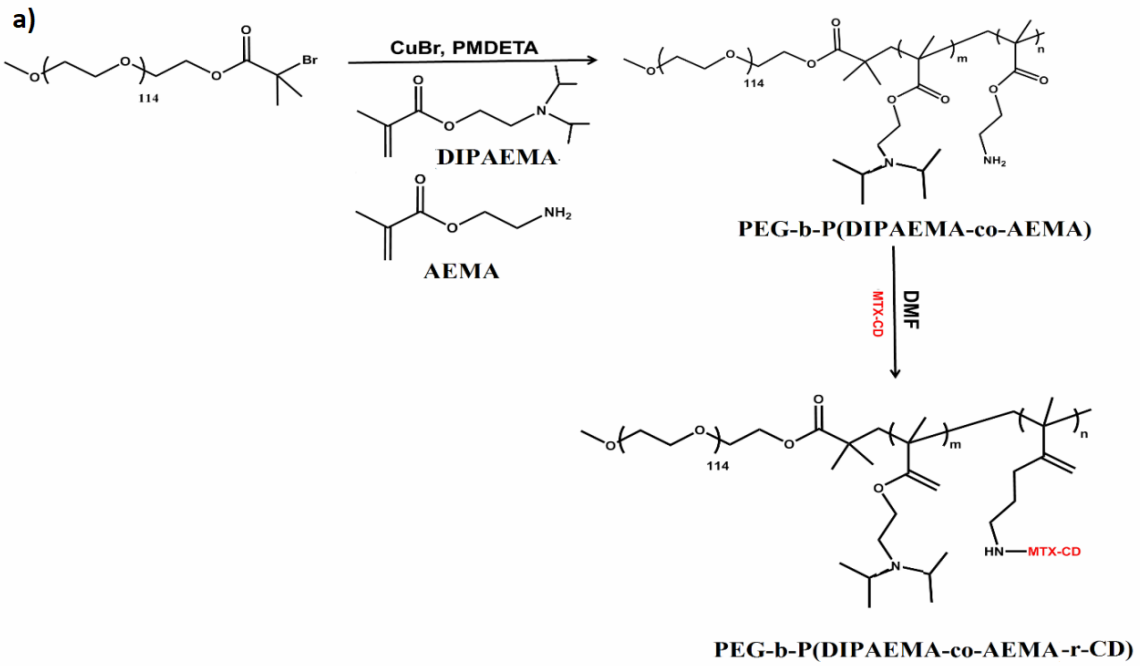

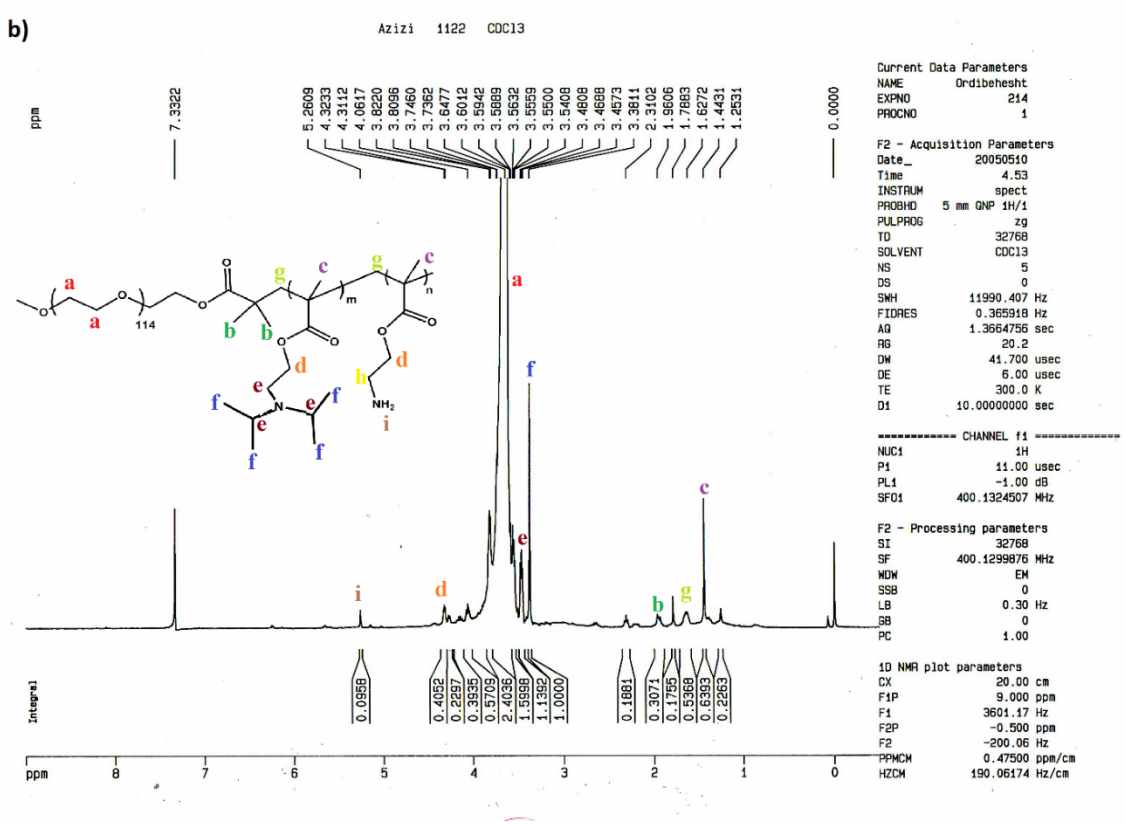

Figure 4. **(a)** Synthetic route of MTX-CD conjugated PEG-b- P(DiPAEMA-co-AEMA). **(b)** ^{1}H NMR spectra of PEG-b- P(DiPAEMA-co-AEMA) in $CDCl_3$, 400Hz, ppm).

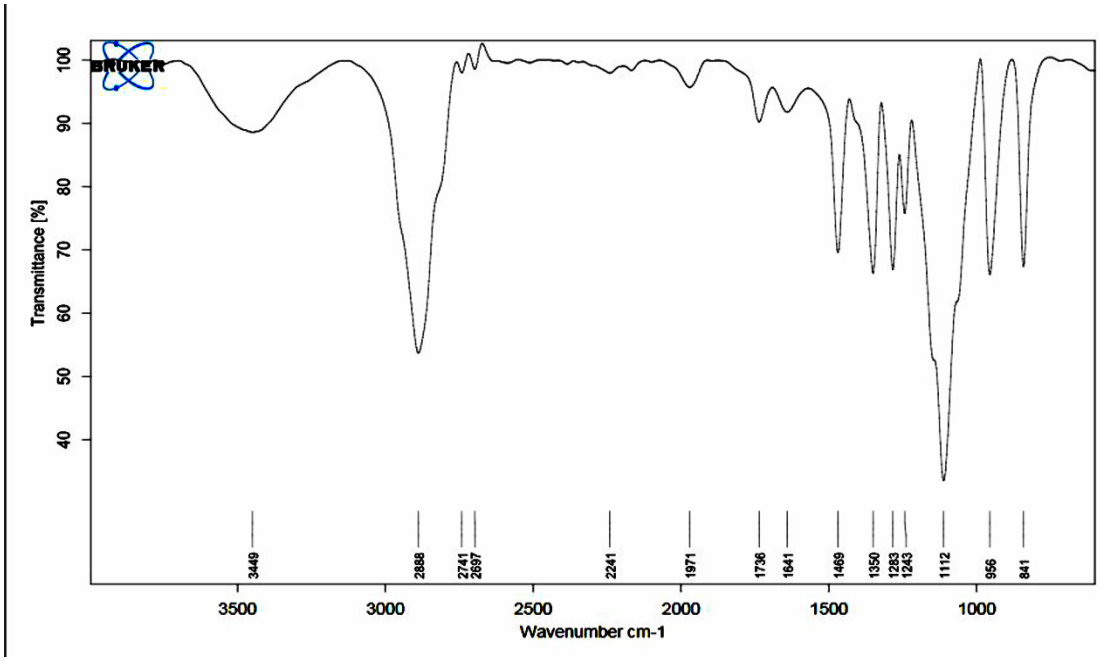

Figure 5. FT-IR spectroscopy of PEG-b-P(DiPAEMA-co-AEMA).

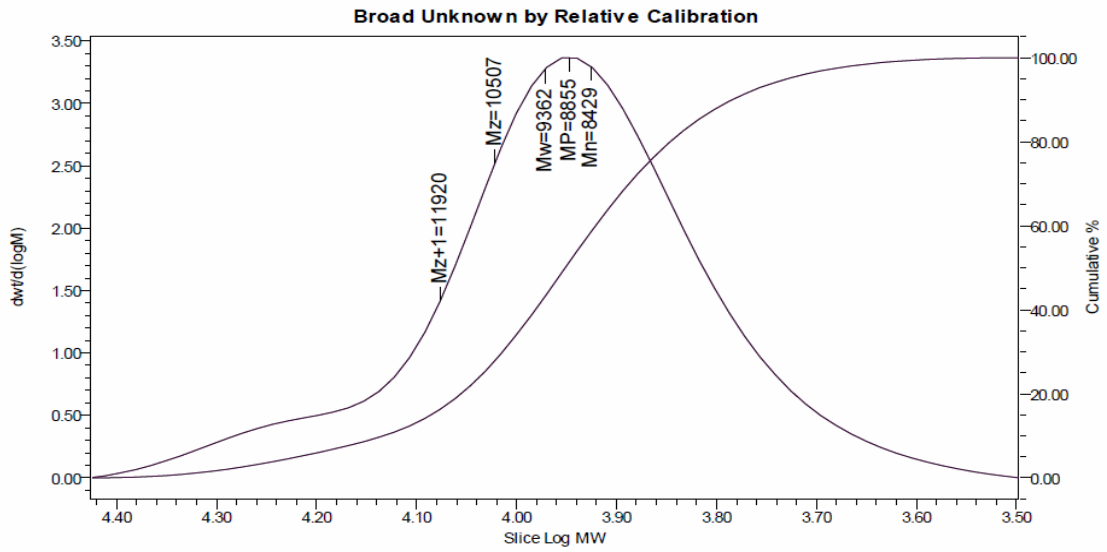

Broad Unknown Relative Peak Table

	Distribution Name	Mn (Daltons)	Mw (Daltons)	MP (Daltons)	Mz (Daltons)	Mz+1 (Daltons)	Polydispersity	Mz/Mw	Mz+1/Mw
1		8429	9362	8855	10507	11920	1.110623	1.122389	1.273318

Figure 6. Molecular weights (Mn and Mw) and polydispersity index (PDI) of PEG-b-P(DiPAEMA-co-AEMA)copolymer obtained by GPC.

3.2 Biocompatibility and cellular uptake of Pol-CD@GNSs-MTX

To analyze the tumoricidal effect of GNSs and Pol-CD@GNSs-MTX on MDA-MB 231 cells and determine IC_{50} values, an MTT assay was performed **(Figure 7).** Data revealed the dose-dependent activity of GNSs and Pol-CD@GNSs-MTX on cancer cells after 24 and 48 hours. The IC_{50} values of GNSs-treated MDA-MB 231 cells were 50 and 100 µg/ml after 24 and 48 hours **(Figure 7 a, b).** We noted that the decoration of GNSs with polymer (Pol-CD@GNSs-MTX) reduced cytotoxic effects. It was estimated that more than 60% of cells were viable after exposure to 100 µg/ml Pol-CD@GNSs-MTX, and this amount reached more than 80% at the concentration of 50 µg/ml **(Figure 7d).** In line with these data, 50 µg/ml Pol-CD@GNSs-MTX was selected for in vitro cell analyses. According to our data, PEG-b-P(DiPAMA-co-

AEMA) copolymer did not exhibit significant cytotoxicity at concentrations up to 50 µg/ml **(Figure 7c).** In concentrations of more than 50 µg/ml, the survival rate of MDA-MB 231 cells was diminished in the group that received 200 µg/ml PEG-b-P(DiPAMA-co-AEMA) near 50% of cells showed cytotoxicity.

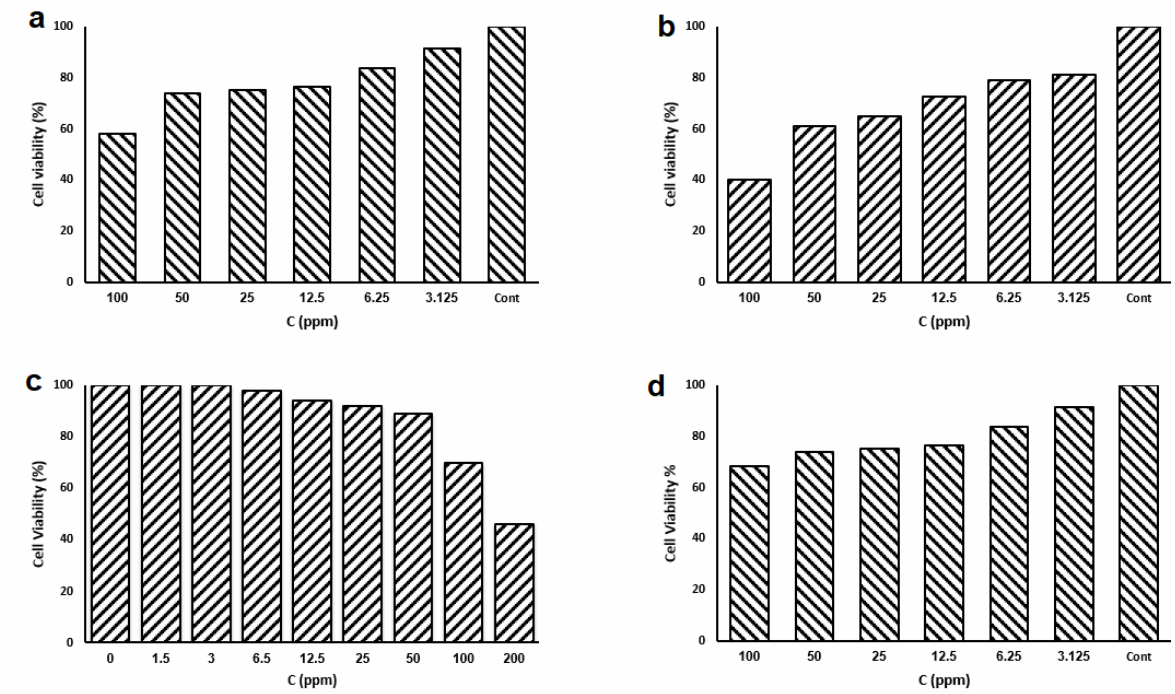

Figure 7. Cell viability of MDA-MB 231 after **(a)** 24 and **(b)** 48h incubation with GNSs. **(c)** PEG-b-P(DiPAMA-co-AEMA) copolymer, and **(d)** Pol-CD@GNSs-MTX in different concentrations.

3.3 Cell Uptake studies

To evaluate the potential role of MTX to target folate receptors and promote cellular uptake, quantitative uptake of Pol-CD@GNSs-MTX was assessed in the MDA-MB 231 cells via flow cytometry **(Figure 8a)** and ICP-MS analyses **(Figure 8b).** According to **Figure 8**, the mean fluorescence intensity (%) of Pol-CD@GNSs-MTX

was significantly higher compared to the Pol-CD@GNSs without MTX (P value<0.001), indicating the higher cellular uptake of MTX and CDs containing formulations due to targeting effect of MTX for folate receptor targeting. Mean fluorescent intensity results showed that 4-hour incubation of cells with Pol-CD@GNSs-MTX led to higher cellular uptake than the matched groups incubated for 1 hour (P value<0.01).

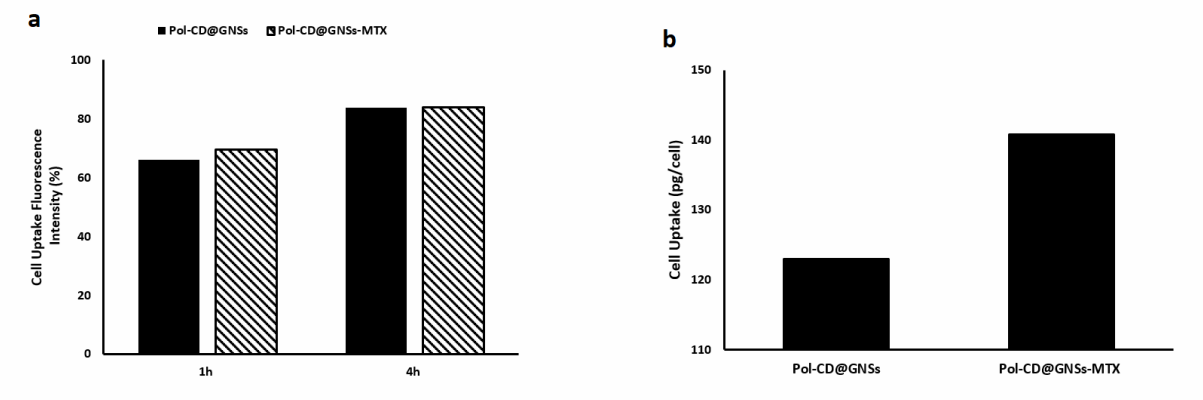

Figure 8.Quantitative cellular uptake analysis: (a) Diagram of mean fluorescence intensity (%) of Pol-CD@GNSs and Pol-CD@GNSs-MTX that uptake by MDA-MB-231 cells in different time intervals: 1 and 4 h, using flow cytometry; (the differences between treatments was statistically significant, $p < 0.001$); (b) ICP-MS (after 4 hours).

3.4 *Synergistic tumoricidal effect of PTT and Pol-CD@GNSs-MTX*

To assess the synergistic tumoricidal effect of PTT and Pol-CD@GNSs-MTX, we measured the photothermal effect by monitoring the changes in temperature of the aqueous phase upon laser irradiation (808 nm, 0.7W/cm^2 for 2-10 minutes). The temperature was not altered in nanoparticle-free media in response to the irradiation **(Figure 9a).** By contrast, 50 µg/ml GNSs and Pol-CD@GNSs-MTX exist in the media culture medium temperature at a similar condition. This effect would be related to the photo-to-heat energy-converting effect of GNSs and Pol-CD@GNSs-MTX after exposure to the NIR laser. The temperature increase was proportional to

the GNSs and Pol-CD@GNSs-MTX concentration and irradiation time. Thus, it was noted that GNSs and Pol-CD@GNSs-MTX can be used as PTT agents in cancer therapy.

Encouraged by the above investigation, we evaluated the NIR laser-induced photothermal oncostatic properties in cancer cells pre-incubated with GNSs. For this purpose, MDA-MB 231 cells were treated with 50 μg/ml GNSs for 4 hours in dark conditions. Then, cells were irradiated for 10 minutes according to the abovementioned protocol. Data showed that the viability of MDA-MB 231 cells decreased drastically and reached about 23% after treatment with GNSs and laser irradiation compared to the non-treated control group **(Figure 9b).** This value declined to 12% in Pol-CD@GNSs-MTX treated group exposed to laser irradiation, indicating synergy of designed nanoparticles and PTT in inhibiting cancer cells. In the group that received laser irradiation, slight but non-significant differences were found regarding cytotoxicity compared to the control group.

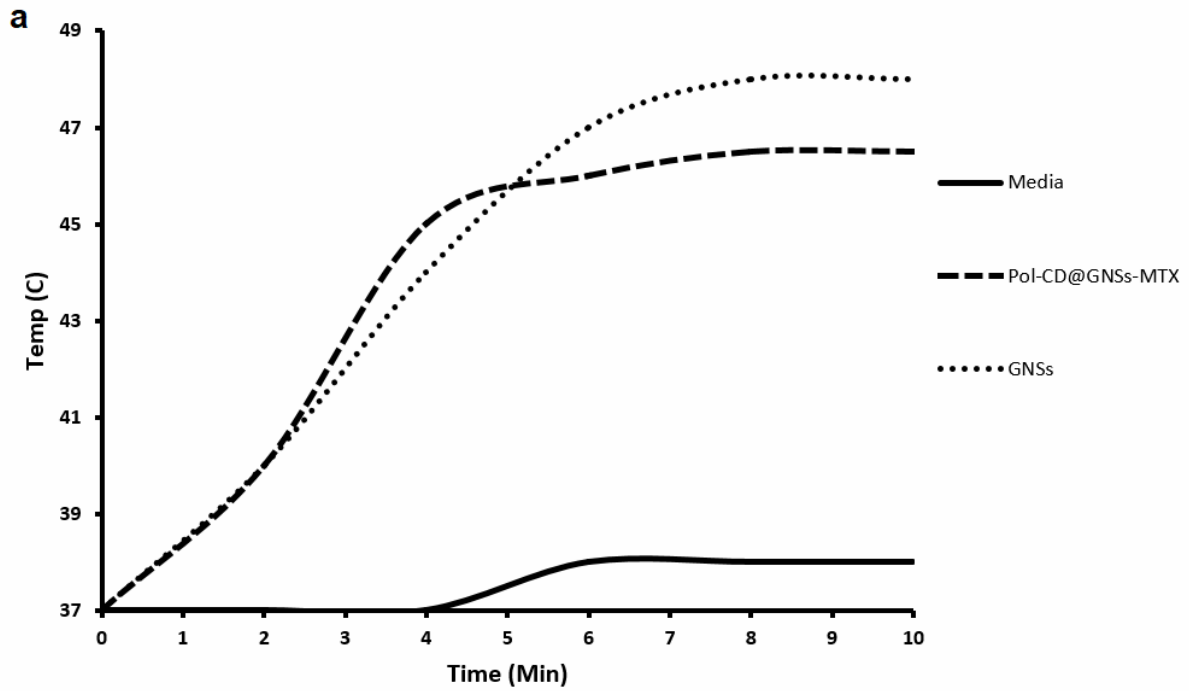

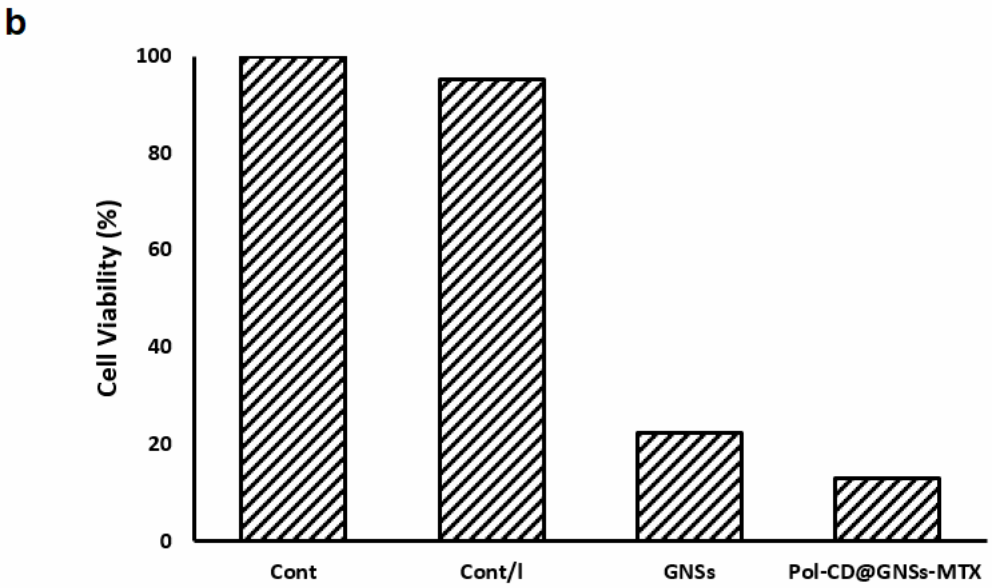

Figure 9. **(a)** The plot of shows photothermal conversion efficiency and time-dependent temperature increase for GNSs, Media, and Pol-CD@GNSs-MTX as a function of irradiation time using an 808 nm laser with the power density of 0.7W/cm^2. **(b)** Cell viability of designed GNSs, Pol-CD@GNSs-MTX all with the concentration of 50 µg/ml along with laser irradiation.

3.5 Combination of Pol-CD@GNSs-MTX and PTT induced apoptosis and prohibited cell growth

The therapeutic properties of GNSs and Pol-CD@GNSs-MTX were determined in MDA-MB 231 cells in the absence and presence of NIR laser using flow cytometric analysis of cell cycle **(Figure 10a-b)** and apoptosis **(Figure 11).** These methods are commonly used to determine DNA duplication in the cell cycle at phases G1, S, and G2/M. Compared to the non-treated control group, in groups that received laser irradiation and MTX alone, about 14 and 18% of the cells were observed in the subG1 phase, respectively. Treatment of cells with Pol-CD@GNSs-MTX alone showed 46% of cancer cells were at the subG1 phase, and this value reached 51% in the group that received laser irradiation and GNSs **(Figure 10a-b).** The irradiation of cells pre-incubated with Pol-CD@GNSs-MTX led to the cycle

arrest of 77% of cells at the subG1 phase. The increase of cell number at the subG1 phase can be associated with apoptotic cell death, leading to reduced cell entry to the G2/M and S phases [31]. In support of this claim, we noted that the percentage of proliferating cells at the G2/M phase was diminished in groups that received the combination of laser irradiation and synthesized nanoparticles.

a

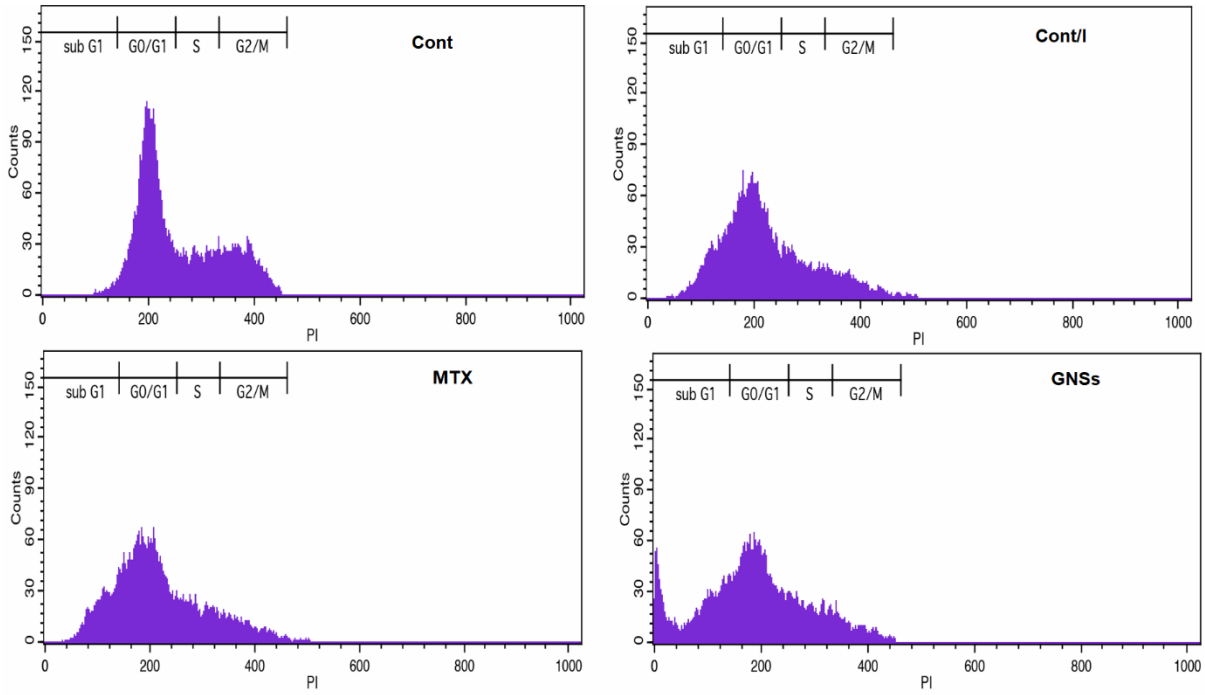

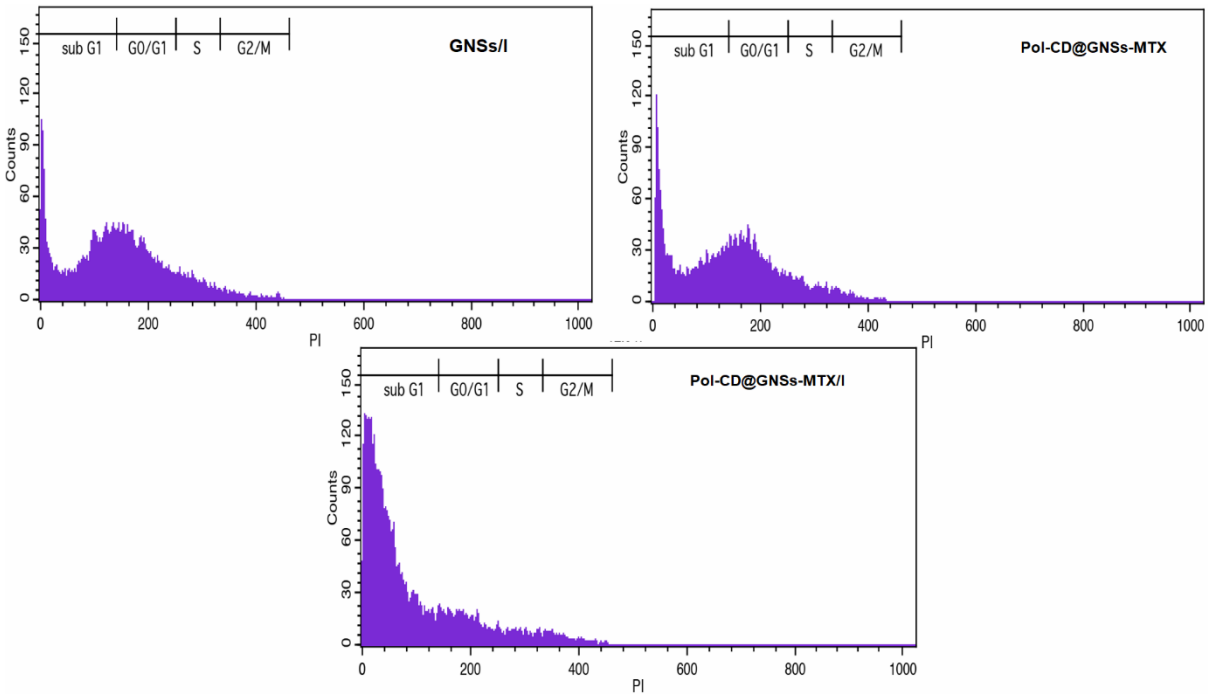

b

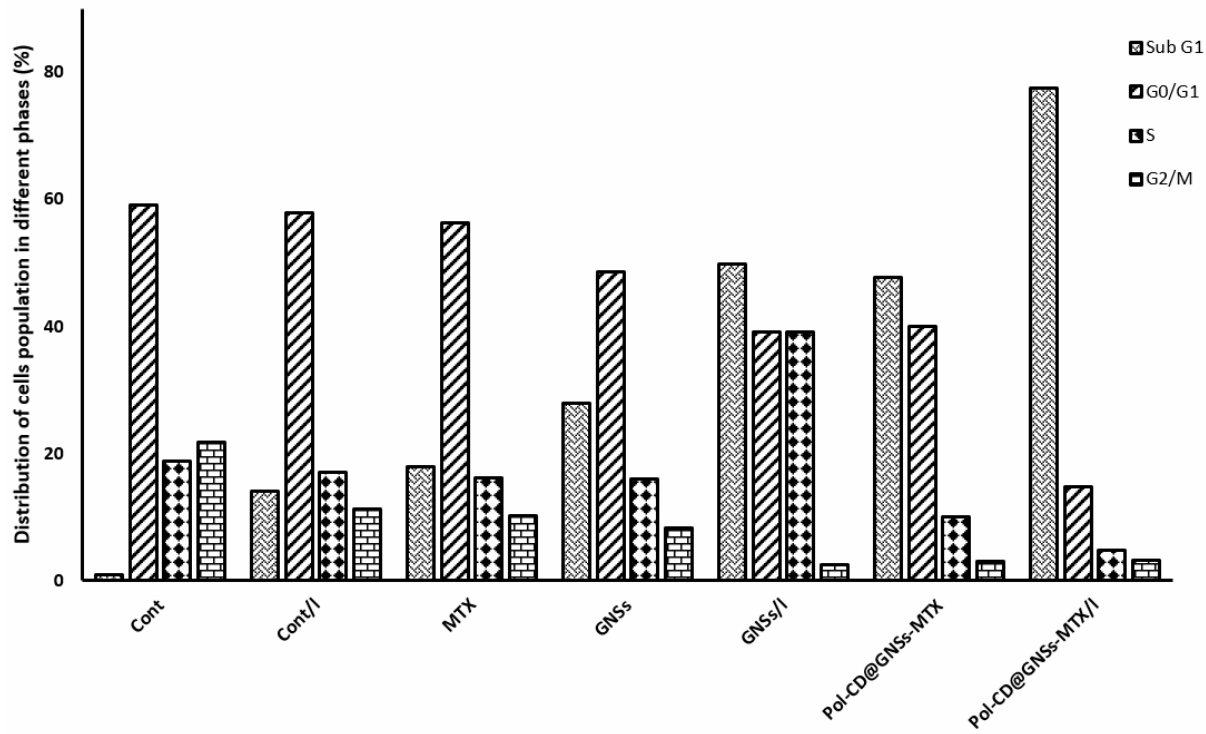

Figure 10. **(a)** Cell cycle arrest analysis using flow cytometry: Effect of Control Laser, MTX, GNSs with laser irradiation, Pol-CD@GNSs-MTX, and Pol-CD@GNSs-MTX with laser irradiation (48 hours)

in the MDA-MB-231 cell cycle. Untreated cells were considered as controls. **(b)** Quantitative percentage of MDA-MB 231 distribution in various cell cycle phases after 48 hours.

An Annexin-V/PI assay was done via flow cytometry to measure the percent of cells with early and late apoptotic changes **(Figure 11).** Data revealed apoptotic and necrotic changes in groups treated with laser irradiation, nanoparticles, or laser irradiation plus nanoparticles. In the group that received laser irradiation alone, we noted that most cell death occurred due to necrosis, reaching 12%. This value was about 21% in cells treated with MTX alone. Irradiation to the cells pre-treated with GNSs led to 52% apoptotic and 40% necrotic death, respectively. It was observed that irradiation to the cells pre-treated with Pol-CD@GNSs-MTX shows 92% apoptosis. Commensurate with our data, late apoptotic changes showed more evident cytotoxic effects in cells receiving Pol-CD@GNSs-MTX and laser irradiation. The higher apoptotic percentage in Pol-CD@GNSs-MTX with laser irradiation groups compared to GNSs with laser irradiation group that were observed in the cell cycle and Annexin-V test is related to their higher cell internalization (proved by flow cytometry and ICP-MS methods). Cell uptake showed a significant role in increasing photothermal efficiency. The amount of heat generation inside the cell is directly related to the number of nanoparticles adsorbed to the cell. This inside the cell destroys the cell.

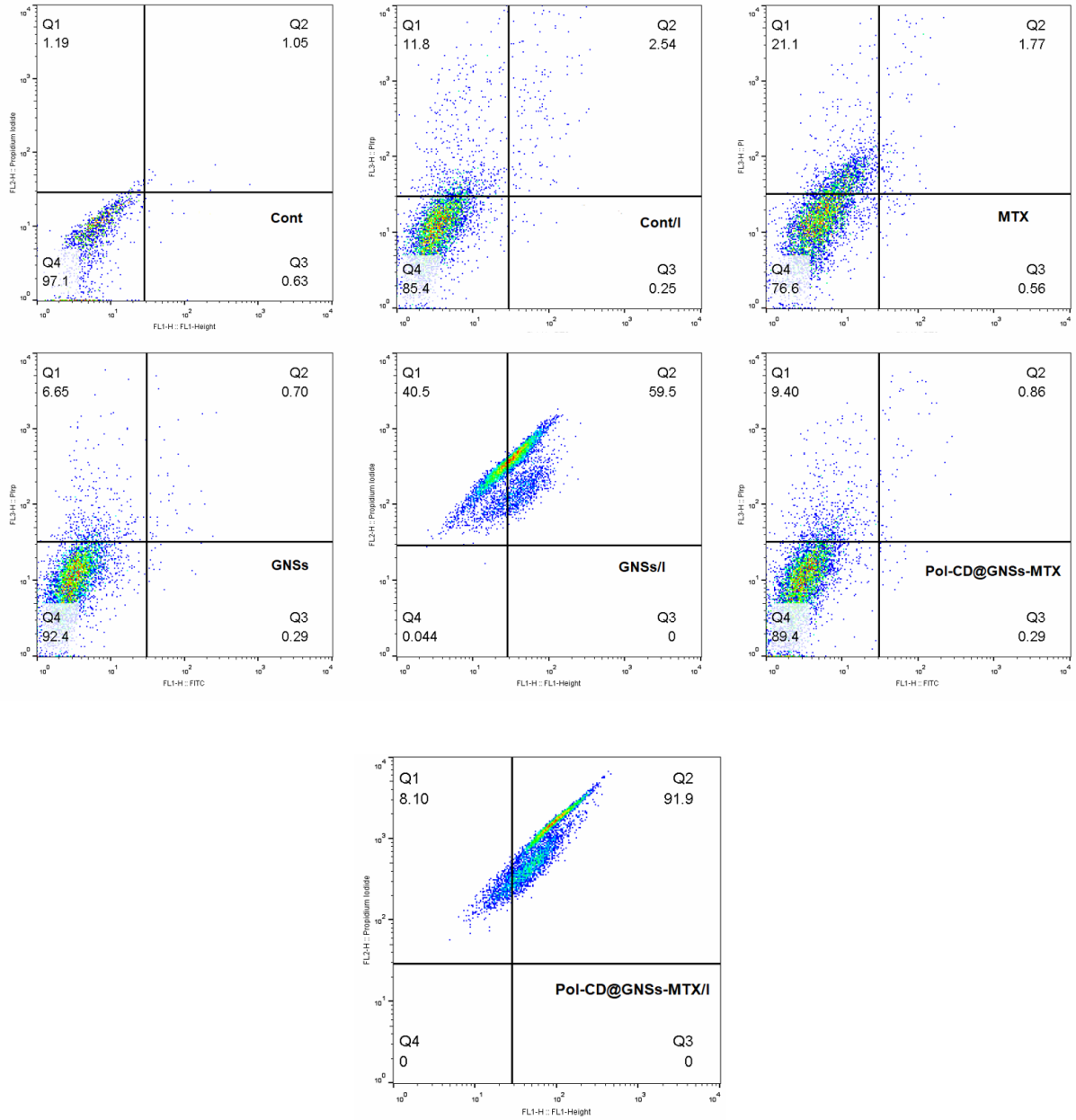

Figure 11. The apoptotic effects of treatments composed of Control Laser, MTX, GNSs with laser irradiation, Pol-CD@GNSs-MTX, and Pol-CD@GNSs-MTX with laser irradiation in MDA-MB-231 cells were determined by flow cytometry. Untreated cells were considered as controls.

Bax, Bcl2, and different Caspase subsets can regulate the apoptotic response [30]. To this end, we measured the expression and protein levels of pro- and anti-apoptotic factors using QRT-PCR analysis and western blotting, respectively. It was

suggested that the expression of Caspase 8 is associated with stimulation of the TNF receptor, showing the stimulation of extrinsic apoptotic response. In contrast, up-regulation of Caspase 9 is related to mitochondrial injury and can trigger an internal apoptosis signaling pathway [32]. In the next step, both Caspase 8 and 9 activate the common apoptosis pathway consisting of Caspase 3, 6, and 7 [30].

In general, we found that the exposure of MDA-MB 231 cells to Pol-CD@GNSs-MTX increased the expression of different pro-apoptotic genes such as Bax, Caspases 3, 7, 8, 9, 10, and 12 compared to the group received only MTX or laser irradiation alone, indicating higher tumoricidal effect of MTX in developed NPs ($p<0.05$) (**Figure 12**). These changes coincided with the reduction of anti-apoptotic effector Bcl-2 ($p<0.05$). These data were by flow cytometry analysis showing enhanced Annexin-V levels in these groups. Heat map analysis exhibited that the expression of apoptosis-related genes was controlled, and laser irradiation (alone) groups were at the minimum levels, showing the lack of apoptotic response compared to other groups. Compared to MTX- and laser-treated cells, the exposure of MDA-MB 231 cells to Pol-CD@GNSs-MTX with laser irradiation yielded maximum apoptotic changes with significant upregulation of Bax, Caspases 3, 7, 8, 9, 10, and 12 and down-regulation of Bcl-2 ($p<0.05$). These data showed that both intrinsic and extrinsic apoptosis signaling pathways were activated in cancer cells exposed to the combination of Pol-CD@GNSs-MTX plus laser groups.

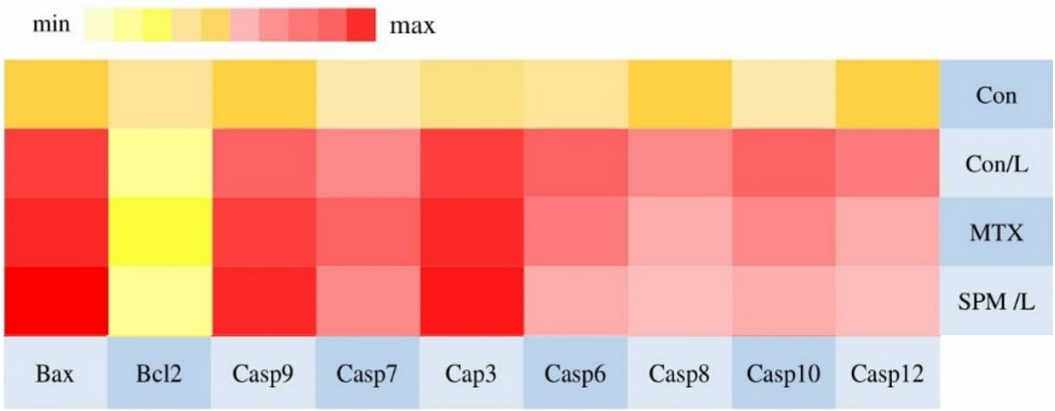
min
max
Con
Con/L
MTX
SPM /L
Bax
Bcl2
Casp9
Casp7
Cap3
Casp6
Casp8
Casp10
Casp12

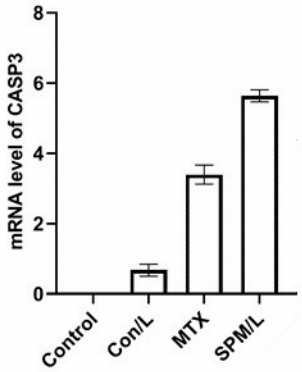
mRNA level of CASP3
Control
Con/L
MTX
SPM/L

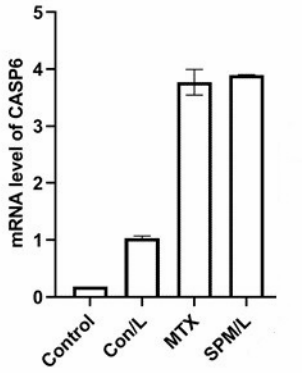
mRNA level of CASP6
Control
Con/L
MTX
SPM/L

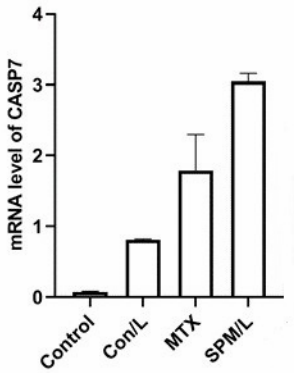
mRNA level of CASP7
Control
Con/L
MTX
SPM/L

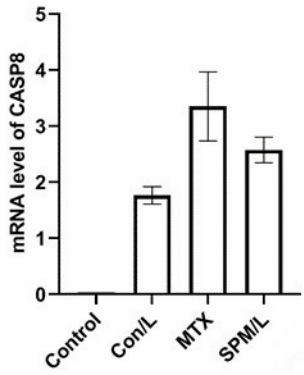
mRNA level of CASP8
Control
Con/L
MTX
SPM/L

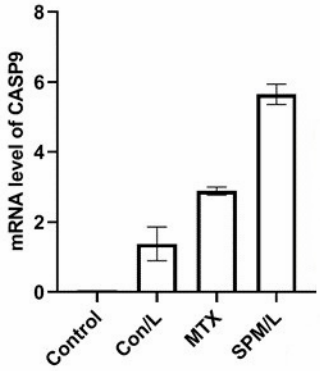
mRNA level of CASP9
Control
Con/L
MTX
SPM/L

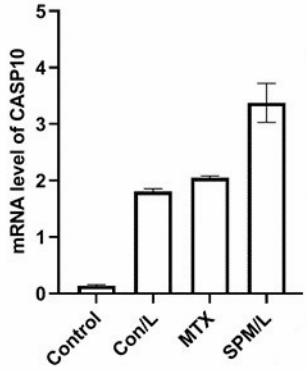
mRNA level of CASP10
Control
Con/L
MTX
SPM/L

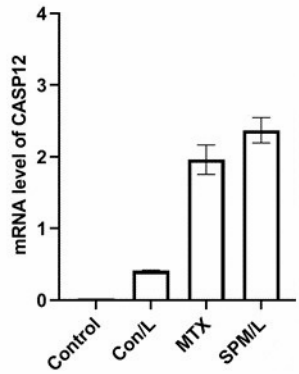
mRNA level of CASP12
Control
Con/L
MTX
SPM/L

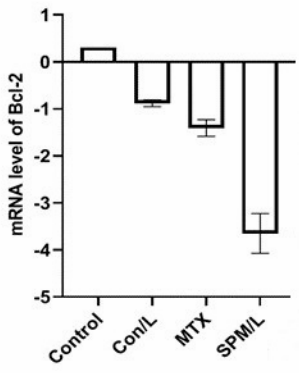
mRNA level of Bcl-2
Control
Con/L
MTX
SPM/L

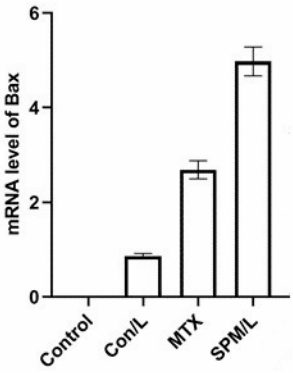
mRNA level of Bax
Control
Con/L
MTX
SPM/L

Figure 12. QRT-PCR expressions of apoptosis pathways. (a)The heat map and (b) graphs depict different ranges of apoptosis pathway expression in MDA-MB-231 cells that were treated with Pol-CD@GNSs-MTX and MTX and laser irradiation. Cells treated with laser only (808 nm, 0.7 W/cm^2, 10 min) were considered positive, and non-treated cells were regarded as negative control. Approximately, Bcl2 depicts down-regulation in all samples. Expression of Bax, Caspases 3 and 9 was increased, which is the benefit of the intrinsic apoptosis pathway. (Con: Control, MTX: Methotrexate, SPM/L: Pol-CD@GNSs-MTX with laser irradiation). All treatment groups showed statistically significant differences compared to control matched-control groups ($0.05<p$ value<0.0001)

Western blot analysis was done to analyze the executive apoptotic protein levels. The outcomes showed that the apoptotic process was initiated by activating Bax, Caspases 3, and 9 **(Figure 13).** Compared to the control group, the protein levels of Bax, Caspases 3, and 9 were increased in Pol-CD@GNSs-MTX with laser irradiation group **(Figure 13).** By contrast, these changes coincided with the suppression of anti-apoptotic protein Bcl-2. Increased cleavage of Caspases 3 and 9 showed the activation of mechanisms related to proteolytic changes in different subcellular locations. In line with these changes, the increase of p53 and p27 and suppression of Bcl-2 showed the inhibition of the cell cycle and subsequent apoptotic changes [33]. A two-fold increase in p27 protein compared with the control can be related to cell cycle arrest following treated Pol-CD@GNSs-MTX with laser irradiation, which is by PI cell cycle analysis.

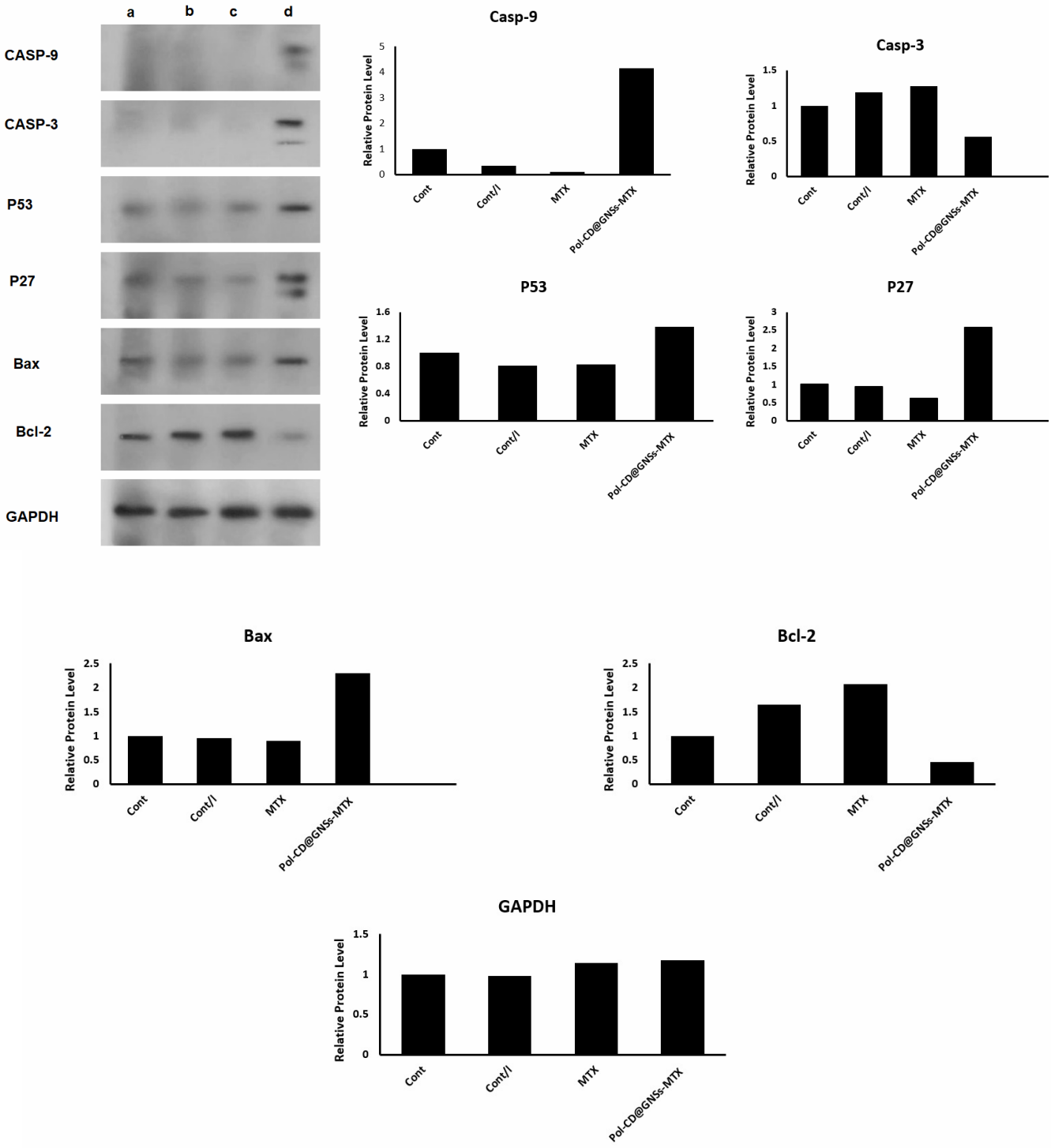

Figure 13. Western blot analysis of different proteins (caspase 3, caspase 9, P27, P53, Bax, Bcl2) regulated by a: Control, b: Control laser, c: MTX, and d: Pol-CD@GNSs-MTX with laser irradation in inducing different apoptotic pathways in MDA-MB 231 cells. GAPDH was considered as a control.

3.6 Cell imaging

Multimodal imaging can incorporate the benefits of all imaging modalities [34]. In this study, multifunctional Pol-CD@GNSs-MTX could combine two modalities: fluorescence and CT imaging. To determine the practicability of Pol-CD@GNSs-MTX for in vitro dual-modality imaging, fluorescence and CT imaging were simultaneously conducted in the MDA-MB 231 cells pre-incubated with Pol-CD@GNSs-MTX **(Figure 14).** A fluorescent image was done in Pol-CD@GNSs-MTX treated cells at different pH values. Fluorescent solid intensity was observed at pH 5.2 and 6.3. In contrast, no detectable fluorescence signal was achieved in higher values (pH 7.4), indicating the crucial importance of pH for activating Pol-CD@GNSs-MTX inside the host cells **(Figure 14b).** The existence of green fluorescence intensity in MDA-MB 231 cells after treatment with Pol-CD@GNSs-MTX can be related to a relatively acidic pH because of active glycolysis mechanisms inside these cells. It is suggested that the normal tissues' pH value is about 7.4. Therefore, in normal conditions (pH >7), the TA groups of poly DiPAEMA segments were deprotonated and self-assemble into the hydrophobic cores of micelles, leading to the quenching of fluorescent signals because the MTX-CDs dyes are close to the GNSs, so their fluorescence is effectively quenched. At lower pH values (5.2 and 6.3), the protonation of TA groups of poly DiPAEMA causes micelle disassembly and an intense intensification in fluorescence emission because of the increase in CD distance to the GNSs. These data were supported by prominent fluorescence activity in Pol-CD@GNSs-MTX-treated MDA-MB 231 cells at pH values of 6.3 and 7.4 **(Figure 14a).** In the meantime, the CT imaging of Pol-CD@GNSs-MTX displays similar trends to fluorescence imaging. As shown in **Figure 14c**, CT signal intensity resulted in brighter images (radiopacity). At adjusted pH (6), no significant difference was detected among the CT signals of Pol-CD@GNSs-MTX-

treated cells. Those results suggest that Pol-CD@GNSs-MTX have excessive perspective for concurrent CT and fluorescence imaging for cancer cells.

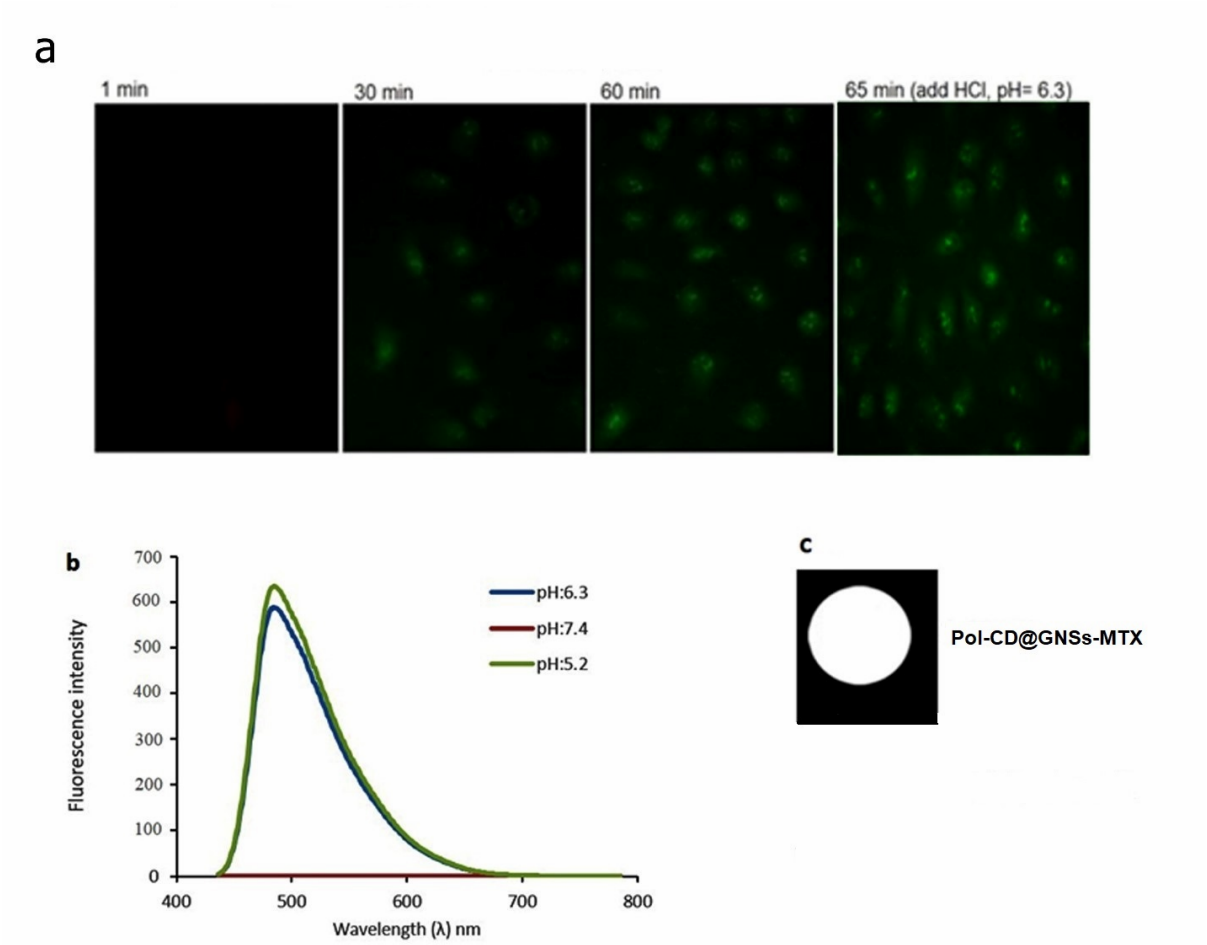

Figure 14. In vitro fluorescence and CT imaging of MDA-MB 231 cells. **(a).** Representative images of activated Pol-CD@GNSs-MTX (pH_t = 6.3 at a concentration of 50 µg/ml)) over time. **(b).** Fluorescence intensity in different pH. **(c).** CT imaging of Pol-CD@GNSs-MTX (pH_t = 6.3). Pol-CD@GNSs-MTX was used at a concentration of 50 µg/ml.

4. Conclusions

In summary, our data showed the multifunctional activity of Pol-CD@GNSs-MTX, and the synthesized nanoparticles can be touted as dual imaging and

therapeutic agents in the tumor niche. It is suggested that the multifunctionality of Pol-CD@GNSs-MTX is based on the activity of GNSs and CDs. In vitro experiments showed that Pol-CD@GNSs-MTX exhibited a strong X-ray attenuation for CT and fluorescence imaging. Moreover, we noted an increased tunable therapeutic efficacy of Pol-CD@GNSs-MTX upon laser irradiation. Pol-CD@GNSs-MTX induced apoptotic cell death in cancer cells exposed to NIR. We believe this multifunctional Pol-CD@GNSs-MTX will have excessive probability in theranostic applications like simultaneous diagnostic imaging and therapy.

Abbreviations

1-Ethyl-3-(3-dimethylaminopropyl) carbodiimide (EDC); 2-(di isopropyl amino) ethyl methacrylate (DiPAEMA); 2-aminoethyl methacrylate (AEMA); 3-(4,5-dimethylthiazol-2-yl)-2,5-diphenyl tetrazolium bromide (MTT); Ascorbic acid (AA); Atom transfer radical polymerization (ATRP); Bovine serum albumin (BSA); Carbon dots (CD); Cetyl trimethyl ammonium bromide (CTAB); Dimethyl aminopyridine (DMAP); Dynamic Light Scattering (DLS); Enhanced tumor penetration and retention (EPR); Fetal bovine serum (FBS); Gel permeation chromatography (GPC); Gold nanorods (GNRs); Gold nanospheres (GNSPhs); Gold nanostars (GNSts); Hydrochloric acid (HCl); Hydrogen tetrachloroaurate (III) hydrate (HAuCl4); Inductively coupled plasma mass spectrometry (ICP-MS); Localized surface plasmon resonance (LSPR); Methotrexate (MTX); N, N, N', N", N"-Pentamethyl diethylenetriamine (PMDETA); Sodium borohydride ($NaBH_4$); Near-infrared (NIR); N-Hydroxysuccinimide (NHS); Photoacoustic tomography (PAT); Photothermal therapy (PTT); Poly (vinyl pyrrolidone) (PVP); Propidium iodide (PI); Proton nuclear magnetic

resonance (^{1}H NMR); Rhodamine B (RhoB); Roswell Park Memorial Institute 1640 growth medium (RPMI); Silver nitrate ($AgNO_3$); Sodium bromide (NaBr); Sodium chloride (NaCl); Sodium sulfide (Na_2S); Tertiary amine (TA); Transmission electron microscopy (TEM); Triethylamine (TEA); X-ray computed tomography (CT).

Ethics approval and consent to participate

Not applicable

Consent for publication

Not applicable

Availability of data and materials

Not applicable

Competing interests

The authors declare that they have no competing interests

Funding

This study was financially supported by grant no. 59950 from Faculty of Advanced Medical Science, Tabriz University of Medical Sciences, Tabriz, Iran.

Authors' contributions

M.A done all parts of experiments, data gathering and participate in manuscript writing. A.P synthesis the gold nanostructures and analysis data related to this part. R.R advised in cell culture experiments and participated in manuscript writing

examination. F.B set up the PTT tests. H.DM help participate in fluorescent imaging of nanoparticles. H.K performed the Rt-qPCR test and analysis this section data. R.S, H.V and M.M are co-supervisors of the project. R.S designed the project, participated in synthesis of polymers, cell culture experiments, data analysis and manuscript writing. H.V participated in data analysis and manuscript writing. M.M participated in imaging data analysis.

Acknowledgments

This study was financially supported by grant no. 59950 from Faculty of Advanced Medical Science, Tabriz University of Medical Sciences, Tabriz, Iran.

5. Reference

1. Xie, J., S. Lee, and X. Chen, *Nanoparticle-based theranostic agents.* Advanced drug delivery reviews, 2010. **62**(11): p. 1064-1079.
2. MacKay, J.A. and Z. Li, *Development of theranostic agents that co-deliver therapeutic and imaging agents.* Advanced drug delivery reviews, 2010. **62**(11).
3. Rai, P., et al., *Development and applications of photo-triggered theranostic agents.* Advanced drug delivery reviews, 2010. **62**(11): p. 1094-1124.
4. Brito, B., et al., *Redox double-switch cancer theranostics through Pt (iv) functionalised manganese dioxide nanostructures.* Nanoscale, 2023. **15**(25): p. 10763-10775.
5. Stephan, M.T., et al., *Therapeutic cell engineering with surface-conjugated synthetic nanoparticles.* Nature medicine, 2010. **16**(9): p. 1035-1041.
6. Verma, A., et al., *Surface-structure-regulated cell-membrane penetration by monolayer-protected nanoparticles.* Nature materials, 2008. **7**(7): p. 588-595.
7. Mayavan, S., et al., *Self-organization, interfacial interaction and photophysical properties of gold nanoparticle complexes derived from resilin-mimetic fluorescent protein rec1-resilin.* Biomaterials, 2011. **32**(11): p. 2786-2796.
8. Schroeder, A., et al., *Treating metastatic cancer with nanotechnology.* Nature Reviews Cancer, 2012. **12**(1): p. 39-50.
9. Yu, H., et al., *pH-and NIR light-responsive micelles with hyperthermia-triggered tumor penetration and cytoplasm drug release to reverse doxorubicin resistance in breast cancer.* Advanced Functional Materials, 2015. **25**(17): p. 2489-2500.
10. Grassberger, C. and H. Paganetti, *Methodologies in the modeling of combined chemo-radiation treatments.* Physics in Medicine & Biology, 2016. **61**(21): p. R344.
11. Zhan, Q., et al., *Engineering blood exosomes for tumor-targeting efficient gene/chemo combination therapy.* Theranostics, 2020. **10**(17): p. 7889.
12. Hu, H., et al., *Nanocolloidosomes with selective drug release for active tumor-targeted imaging-guided photothermal/chemo combination therapy.* ACS applied materials & interfaces, 2017. **9**(48): p. 42225-42238.
13. Yang, H.W., et al., *Non-invasive synergistic treatment of brain tumors by targeted chemotherapeutic delivery and amplified focused ultrasound-hyperthermia using magnetic nanographene oxide.* Advanced materials, 2013. **25**(26): p. 3605-3611.
14. Kim, J.-W., et al., *Golden carbon nanotubes as multimodal photoacoustic and photothermal high-contrast molecular agents.* Nature nanotechnology, 2009. **4**(10): p. 688-694.
15. Zhi, D., et al., *Photothermal therapy.* Journal of Controlled Release, 2020.
16. Chen, Y., et al., *Nanomaterials-based photothermal therapy and its potentials in antibacterial treatment.* Journal of Controlled Release, 2020.
17. Dreaden, E.C., et al., *The golden age: gold nanoparticles for biomedicine.* Chemical Society Reviews, 2012. **41**(7): p. 2740-2779.
18. Bardhan, R., et al., *Theranostic nanoshells: from probe design to imaging and treatment of cancer.* Accounts of chemical research, 2011. **44**(10): p. 936-946.
19. Xia, Y., et al., *Gold nanocages: from synthesis to theranostic applications.* Accounts of chemical research, 2011. **44**(10): p. 914-924.
20. Srivatsan, A., et al., *Gold nanocage-photosensitizer conjugates for dual-modal image-guided enhanced photodynamic therapy.* Theranostics, 2014. **4**(2): p. 163.

21. Azizi, M., et al., *Synthesis of Self-Targeted Carbon Dot with Ultrahigh Quantum Yield for Detection and Therapy of Cancer.* ACS omega, 2020. **5**(38): p. 24628-24638.
22. Yuan, H., et al., *Spectral characterization and intracellular detection of Surface-Enhanced Raman Scattering (SERS)-encoded plasmonic gold nanostars.* Journal of Raman spectroscopy, 2013. **44**(2): p. 234-239.
23. Liu, Y., et al., *A plasmonic gold nanostar theranostic probe for in vivo tumor imaging and photothermal therapy.* Theranostics, 2015. **5**(9): p. 946.
24. Zhou, K., et al., *Tunable, ultrasensitive pH-responsive nanoparticles targeting specific endocytic organelles in living cells.* Angewandte Chemie International Edition, 2011. **50**(27): p. 6109-6114.
25. Chen, Y.-H., et al., *Methotrexate conjugated to gold nanoparticles inhibits tumor growth in a syngeneic lung tumor model.* Molecular pharmaceutics, 2007. **4**(5): p. 713-722.
26. Dong, B., et al., *Reversible self-assembly of nanoprobes in live cells for dynamic intracellular pH imaging.* ACS nano, 2019. **13**(2): p. 1421-1432.
27. Espinosa, A., et al., *Cancer cell internalization of gold nanostars impacts their photothermal efficiency in vitro and in vivo: toward a plasmonic thermal fingerprint in tumoral environment.* Advanced healthcare materials, 2016. **5**(9): p. 1040-1048.
28. Nergiz, S.Z., et al., *Multifunctional hybrid nanopatches of graphene oxide and gold nanostars for ultraefficient photothermal cancer therapy.* ACS applied materials & interfaces, 2014. **6**(18): p. 16395-16402.
29. Rahimi, M., et al., *Dendritic chitosan as a magnetic and biocompatible nanocarrier for the simultaneous delivery of doxorubicin and methotrexate to MCF-7 cell line.* New Journal of Chemistry, 2017. **41**(8): p. 3177-3189.
30. Rahmani, A., et al., *Novel pH-sensitive and biodegradable micelles for the combined delivery of doxorubicin and conferone to induce apoptosis in MDA-MB-231 breast cancer cell line.* RSC Advances, 2020. **10**(49): p. 29228-29246.
31. Sabzi, A., et al., *Targeted co-delivery of curcumin and doxorubicin by citric acid functionalized Poly (ε-caprolactone) based micelle in MDA-MB-231 cell.* Colloids and Surfaces B: Biointerfaces, 2020. **194**: p. 111225.
32. Han, J.-H., et al., *Regulation of Caspase-8 Activity at the Crossroads of Pro-Inflammation and Anti-Inflammation.* International Journal of Molecular Sciences, 2021. **22**(7): p. 3318.
33. Kandhavelu, J., et al., *A novel EGFR inhibitor, HNPMI, regulates apoptosis and oncogenesis by modulating BCL-2/BAX and p53 in colon cancer.* British Journal of Pharmacology, 2023.
34. Li, X.-D., et al., *Imaging guided photothermal therapy using iron oxide loaded poly (lactic acid) microcapsules coated with graphene oxide.* Journal of Materials Chemistry B, 2014. **2**(2): p. 217-223.